ChemComm

ROYAL SOCIETY OF CHEMISTRY

FEATURE ARTICLE

View Article Online
View Journal | View Issue

Cite this: *Chem. Commun.*, 2023, **59**, 5823

Recent advances in zinc–air batteries: self-standing inorganic nanoporous metal films as air cathodes

Jinfa Chang [a] and Yang Yang *[abcde]

Zinc–air batteries (ZABs) have promising prospects as next-generation electrochemical energy systems due to their high safety, high power density, environmental friendliness, and low cost. However, the air cathodes used in ZABs still face many challenges, such as the low catalytic activity and poor stability of carbon-based materials at high current density/voltage. To achieve high activity and stability of rechargeable ZABs, chemically and electrochemically stable air cathodes with bifunctional oxygen reduction reaction (ORR)/oxygen evolution reaction (OER) activity, fast reaction rate with low platinum group metal (PGM) loading or PGM-free materials are required, which are difficult to achieve with common electrocatalysts. Meanwhile, inorganic nanoporous metal films (INMFs) have many advantages as self-standing air cathodes, such as high activity and stability for both the ORR/OER under highly alkaline conditions. The high surface area, three-dimensional channels, and porous structure with controllable crystal growth facet/direction make INMFs an ideal candidate as air cathodes for ZABs. In this review, we first revisit some critical descriptors to assess the performance of ZABs, and recommend the standard test and reported manner. We then summarize the recent progress of low-Pt, low-Pd, and PGM-free-based materials as air cathodes with low/non-PGM loading for rechargeable ZABs. The structure–composition–performance relationship between INMFs and ZABs is discussed in-depth. Finally, we provide our perspectives on the further development of INMFs towards rechargeable ZABs, as well as current issues that need to be addressed. This work will not only attract researchers' attention and guide them to assess and report the performance of ZABs more accurately, but also stimulate more innovative strategies to drive the practical application of INMFS for ZABs and other energy-related technologies.

Received 16th February 2023,
Accepted 19th April 2023

DOI: 10.1039/d3cc00742a

rsc.li/chemcomm

[a] *NanoScience Technology Center, University of Central Florida, Orlando, FL 32826, USA. E-mail: Yang.Yang@ucf.edu*
[b] *Department of Materials Science and Engineering, University of Central Florida, Orlando, FL 32826, USA*
[c] *Renewable Energy and Chemical Transformation Cluster, University of Central Florida, Orlando, FL 32826, USA*
[d] *Department of Chemistry, University of Central Florida, Orlando, FL 32826, USA*
[e] *The Stephen W. Hawking Center for Microgravity Research and Education, University of Central Florida, Orlando, FL 32826, USA*

Jinfa Chang

Prof. Jinfa Chang received his PhD degree in physical chemistry in 2018, from the Chinese Academy of Sciences (CAS), Changchun Institute of Applied Chemistry (CIAC). Afterward, he served as a special postdoctoral researcher at AIST-Kyoto University from 2018 to 2019. He then became a postdoctoral researcher in Dr Yang's team, backed by the preeminent postdoctoral program (P3) in 2019. He became a full professor at Northeast Normal University in March 2023. Prof. Chang is primarily interested in electrochemical energy storage and conversion.

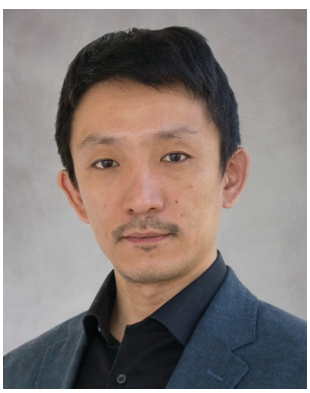

Yang Yang

Prof. Yang Yang is an associate professor at the University of Central Florida. His research focuses include surface and interface electrochemistry of energy materials and devices, nanomanufacturing, electrochemical engineering, nanoscience technology, and advanced thin-film technologies. His website can be found at ***https://www.yangyanglab.com.***

1. Introduction

Many emerging electrochemical energy systems (EESs) such as Li-ion batteries (LIBs) and fuel cells have been substantially developed to replace conventional fossil energy,[1–5] due to their renewable, low-carbon, eco-friendly, and high-performance features.[6–9] Since EESs have been widely used in our daily life, including in smartphones, laptops, electric vehicles, smart grids, aerospace, mobile power supply, *etc.*, the reliability and safety concerns of EESs are attracting increasing research attention in recent years.[10,11] As a representative family member of metal–air batteries delivering high energy, zinc–air batteries (ZABs)[12–14] are known for high safety and have emerged as the most prominent MABs[15] due to the suitable theoretical voltage, specific/volumetric energy density, and specific capacity[16] (Fig. 1). ZABs have attracted increasing attention from researchers and almost exponential growth in ZAB publications was achieved in the past decade (Fig. 2).

Even though significant progress has been achieved for ZABs, we should keep in mind that there are still some problems that are hindering the further development of ZABs and large-scale commercialization. The air electrode, used as a cathode in ZABs, faces many challenges, such as the sluggish kinetic reaction rate for both the oxygen reduction reaction (ORR) and oxygen evolution reaction (OER), which is accompanied by a 4-electron(e) pathway.[15] In addition, the commonly used air-electrode catalyst with powder materials usually faces the problem of blocking active sites, low surface area, and blocking or unordered porous channels that hinder mass and ion transport during the reaction. While the binder and additive, such as Nafion and PTFE solutions, are needed to support the powder catalysts on conductive substrates, which may block the active sites of the catalysts, increase the thickness and interface resistance of the catalytic layer, and finally result in poor performance but with much lower PGM utilization and high cost. Thus, it is urgent to develop alternative materials for the air electrode with high PGM utilization, anti-corrosive and stable abilities under harsh conditions, and a high surface with plenty of available active sites, pore channels, and self-standing structures.

Inorganic nanoporous metal films (INMFs) are a typical component widely used in renewable energy storage and transformation technology that meet all the requirements for air-electrodes in ZABs.[11,17,18] Compared to traditional powder materials used as catalysts in air electrodes, INMFs offer a lot of advantages and unique merits. These include high surface area, three-dimensional channels, and a porous structure with controllable crystal growth facet/direction. Firstly, the high surface area of INMFs provides plenty of active sites and enables maximum atomic utilization, particularly with PGMs, which are expensive, ultimately reducing the cost of ZABs. Secondly, the three-dimensional channels with an ordered structure or direction promote the mass/ion transport during the electrocatalytic reactions. Thirdly, the porous structure of INMFs effectively relieves the stress generated by volume variations and can be seamlessly integrated with handheld electronic devices. Fourthly, the controllable crystal growth facet/direction of INMFs enables scientists to study the structure–composition–performance relationship, thus screening the optimized materials for air electrodes in ZABs. Finally, the unique self-standing character of INMFs allows them to be used directly as air electrodes without other conduction substrates such as carbon paper and cloth, thus saving on the binder/additive (such as Nafion and PTFE solutions) needed for powder catalysts. This approach reduces interface resistance, decreases the thickness of the catalytic layer, exposes the maximum active sites, and reduces the integration cost of ZABs. Therefore, INMFs have been widely used as air electrodes in ZABs.

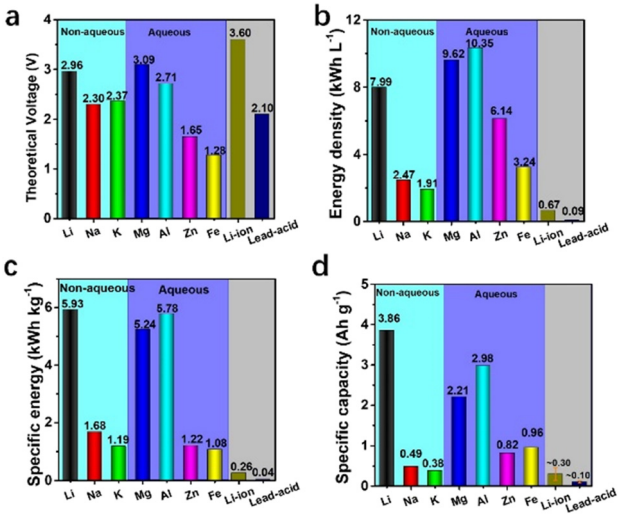

Fig. 1 (a) Theoretical voltage, (b) energy density, (c) specific energy, and (d) specific capacity between metal–air batteries, lead–acid batteries, and lithium-ion batteries. Reproduced with permission from ref. 15 Copyright 2021 Wiley-VCH GmbH.

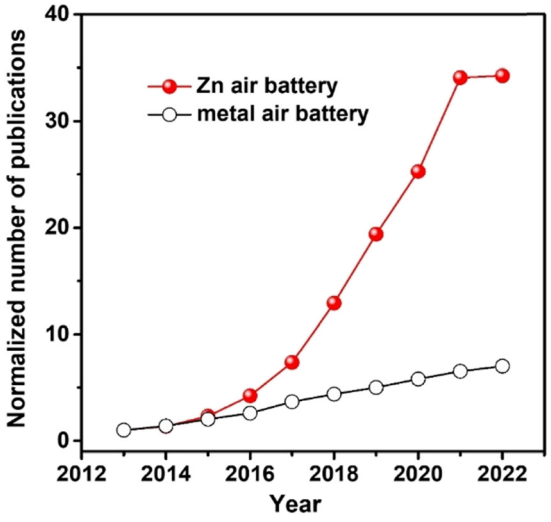

Fig. 2 Normalized publication trends of ZABs and metal–air batteries (MABs) in the recent decade. The publication number in 2012 was normalized as 1. Almost exponential growth was found for ZABs. The counts were obtained from the Web of Science.

Since the metal anode in ZABs has been well studied and reviewed in previous work by our group and other groups,[15,19–26] the key point of this review is to focus on air cathodes in ZABs. Besides, the method to prepare the INMFs was also well summarized previously,[17,18] thus, the synthetic methods towards INMFs are also omitted. In this paper, we first revisit the critical descriptors to assess the performance of ZABs. The recent progress of INMFs as self-standing air electrodes with low/non-PGM loading for rechargeable ZABs was then analyzed and summarized. The structure–composition–performance relationship between INMFS and ZABs is discussed in-depth. Finally, the current issues that need to be addressed and perspectives on the further development of INMFs towards rechargeable ZABs are given. This review provides a more impartial performance comparison in the ZAB field and will inspire more researchers to commit to the development of high-performance and robust INMF air electrodes for ZABs.

2. Fundamentals of ZABs

2.1. Working principles and open circuit voltage

A typical ZABs consists of a Zn anode, separators, and an air cathode (Fig. 3).[15,21,27–29] To ensure the successful operation of ZABs, a high concentration of potassium hydroxide (KOH, 6 M) aqueous solution is usually used to reduce system resistance.[21,30,31] The separator is soaked in KOH solution to separate the anode and cathode, preventing short circuits in ZABs.[32] It should be noted that besides the aqueous electrolyte (Fig. 1), other types of electrolytes, such as molten salt electrolytes,[33] polymer electrolytes,[34] all-solid-state electrolytes,[35–37] *etc.* have appeared that may replace water electrolytes. These types of non-aqueous electrolytes can avoid the common issues that aqueous alkaline electrolytes faced, such as hydrogen evolution, Zn dendrite formation, carbonate precipitation, and so on. However, these non-aqueous-based ZABs usually have a much higher system resistance and need to be operated under high temperatures (550 °C).[33] Thus, the most widely studied and used ZABs are still based on aqueous electrolytes. During the discharge process, the Zn anode loses 2 electrons and is oxidized to Zn^{2+}, which further reacts with OH^- to form $Zn(OH)_4^{2-}$ (eqn (1) and (2)). Simultaneously, two electrons are transferred from the anode to the cathode through the external circuit, and O_2 is reduced to OH^- (ORR) on the cathode side of ZABs (eqn (3)).[29,32] The potential is *versus* the standard hydrogen electrode (SHE). During the charging process, OH^- loses electrons and is oxidized to O_2 at the air cathode side (OER), while ZnO captures electrons, and Zn is redeposited on the anode side.[15]

Zn anode electrooxidation:

$$Zn + 4OH^- \rightarrow Zn(OH)_4^{2-} + 2e^- \quad E = -1.25\ V_{SHE} \tag{1}$$

$$Zn(OH)_4^{2-} \rightarrow ZnO(s) + 2H_2O + 2OH^- \tag{2}$$

Oxygen cathode electroreduction:

$$O_2 + 2H_2O + 4e^- \rightarrow 4OH^- \quad E = 0.4\ V_{SHE} \tag{3}$$

The overall reaction:

$$O_2 + 2Zn \rightarrow 2ZnO \quad E = 1.65\ V_{SHE} \tag{4}$$

The theoretical open circuit voltage (OCP) or maximum voltage of a single ZAB is about 1.65 V.[15,29] The OCP is an important activity descriptor of ZABs, as it can indicate if the ZABs are under short-circuited conditions. Additionally, a high OCP indicates that the air cathode has high ORR activity, since the same Zn foil/plate is used, and the same reaction occurred at the anode. It should be noted that when reporting the OCP of ZABs, steady-state conditions should be acquired first to avoid the reported value being over-estimated due to the contribution of capacitance and transient voltage. The steady-state conditions of ZABs can usually be obtained by testing the OCP using an electrochemical workstation for 1 hour.[38,39]

2.2. Power density, rechargeability, and round-trip overpotentials

The power density at specific potentials can be calculated using the polarization curve by multiplying the corresponding current density and voltage.[14,40–42] The power density is a crucial activity descriptor for ZABs, and good ZABs should have a relatively high power density.[43–46] In the case of rechargeable ZABs, the air electrode must possess good OER activity to minimize the charge/discharge potential gap (or round-trip overpotentials) for optimal performance.[47] It is strongly recommended to report the power density of ZABs during steady-state conditions.

2.3. Specific capacity and Zn utilization ratio

Different from LIBs, the discharge capacity of ZABs is estimated by considering the consumed anode mass after a full discharge process (eqn (5)).[21]

$$\text{Specific capacity (SC)} = \frac{i \times t}{M_{Zn(con)}} = \frac{i \times t}{M_{Zn(ini)} - M_{Zn(res)}} \tag{5}$$

where i and t are the discharge current (mA) and time (hours), respectively. The consumed mass ($M_{Zn(con)}$) of Zn anodes is estimated by measuring the weight change before ($M_{Zn(ini)}$) and after ($M_{Zn(res)}$) the full discharging.

While the Zn utilization ratio (ZUR) is defined as eqn (6),[24]

$$ZUR = \frac{SC_{test}}{SC_{ideal}} \times 100\% \tag{6}$$

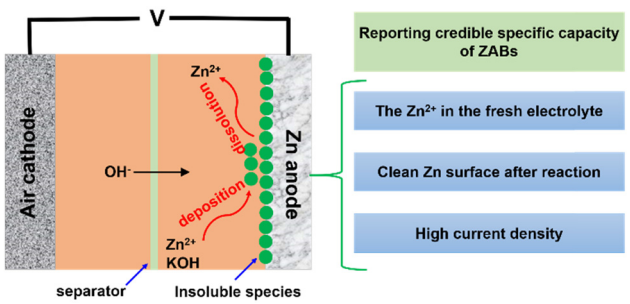

Fig. 3 The schematic illustration depicts the operating principle of ZABs, and the proposed methods to report an accurate and credible specific capacity of ZABs.

where the SC_{test} is the experimental test SC, while the SC_{ideal} is the ideal or theoretical value of ZABs (820 mA h g^{-1}, Fig. 1d). However, the discharge capacity and ZUR could likely be overestimated[48–51] in practice because of the lack of a high-precision method to measure the mass change and the difficulty in cleaning the discharged anodes to remove all unwanted by-products firmly adhered to the anode surface.

The formation and composition of by-products vary with the side reactions occurring at the anode/electrolyte interface,[52] which depend on the local electrochemical conditions (Fig. 4) such as the composition of the electrolyte, local pH, applied potential, *etc.* For instance, in ZABs using alkaline electrolytes (mostly high concentration 6 M KOH to ensure high ionic conductivity), Zn could be passivated by forming an insoluble and stubborn zinc oxide on the surface[53] (eqn (2) and Fig. 4). In addition, zinc acetate is usually added to the electrolytes to improve the reduction of Zn^{2+} during the charging process,[54,55] improving the cyclability of ZABs. Even though the Zn corrosion rate in basic solutions is slow, however, the hydrogen evolution reaction (HER) also occurred with H_2 gas generated during the discharge process (eqn (7)), which result in charge losses and potential explosion due to the H_2 accumulation.[55]

$$Zn + 2H_2O \rightarrow Zn(OH)_2 + H_2 \quad (7)$$

Thus, a suitable concentration of KOH should be selected to minimize the Zn corrosion and HER.[55] And it is reported that 30% KOH aqueous solution is a good choice[56] that coordinates and compromises the ionic conductivity, ZnO solubility, and Zn corrosion.

It is clear that after the discharge process, the residual species on the Zn anode surface are compounds that contain Zn metal, the insoluble zinc oxide (ZnO) or $Zn(OH)_2$. Most importantly, the Zn metal, as well as ZnO and $Zn(OH)_2$ derived from the zinc acetate added in the electrolyte, may be overlooked during the calculation of the initial mass of Zn; in addition, the Zn plate or foil after discharge may not be washed thoroughly, leading to the adhesion of ZnO and $Zn(OH)_2$ on the Zn surface and thus resulting in the inaccurate estimation of the consumed Zn after discharging.

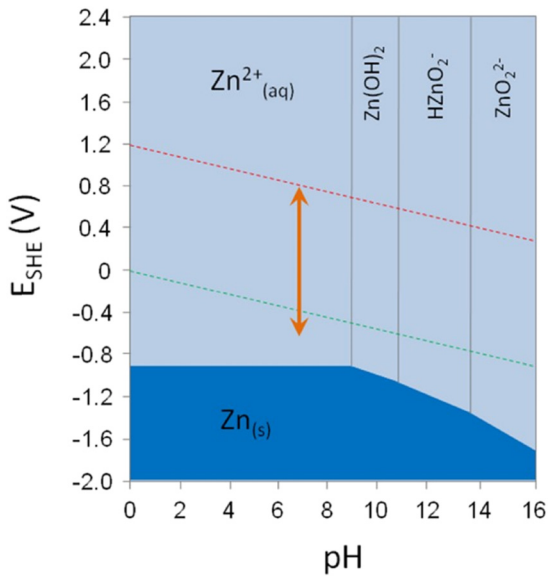

Fig. 4 Pourbaix diagram of zinc. Red and green dashed lines represent the reduction reactions of O_2 and H^+, respectively. Adapted with permission from ref. 52 Copyright 2017, Elsevier.

Besides, the current density selected for the discharging test may also influence the calculated specific capacity and ZUR (as shown in Table 1). When the applied current density is too small (less than 10 mA cm^{-2}), the non-Faradic current arising from the capacitive contribution cannot be neglected. The portion of capacitive current was found to decrease with increasing the applied current density above 10 mA cm^{-2},[57] or even higher.[58] Thus it would be much better to use a high current density to minimize the contribution from the non-Faradic current when evaluating the specific capacity.

In all, we would like to suggest considering the effect of zinc acetate (or other Zn^{2+} in the electrolyte as an additive) in the calculation of the specific capacity and ZUR (Fig. 3). In addition, the insoluble ZnO or $Zn(OH)_2$ on the Zn metal surface should be thoroughly removed by polishing, ultrasound treatment, and washing. Furthermore, the high current density is recommended for the accurate estimation of the specific capacity to eliminate the contribution from the capacitive current. Through these suggested means, the specific capacity and ZUR of ZABs and other MABs can be calculated more accurately.

2.4. Mass/volume energy density of ZABs

The energy density of ZABs describes the amount of energy that can be stored in ZABs per mass or volume.[21] Thus, the energy density of ZABs can be divided into two types: the mass/gravimetric energy density and volumetric energy density, respectively, with units of energy per kg (W h kg^{-1}) and energy per liter (W h L^{-1}). The mass/gravimetric energy density can be calculated as follows:

$$\text{Mass energy density (Wh kg}^{-1}) = \frac{F \times n \times \text{OCP}}{3.6}\left(\frac{\ln(M_{M+O}/M_{Metal})}{M_{M+O} - M_{Metal}}\right) \quad (8)$$

where F is the Faraday constant, n is the number of electrons transferred per Zn ion, OCP is the ZABs's nominal voltage, M_{Metal} is the molar mass of the Zn anode and M_{M+O} is the combined molar mass of the metal anode and the stoichiometric amount of oxygen that enters the battery.

While for volumetric energy density, it is calculated using the density of the anode in its most favorable oxidized phase, since the volume of ZABs must accommodate the associated volume expansion of this phase from the metallic form. The volumetric energy density can be calculated as:

$$\text{Volumetric energy density (W h L}^{-1}) = (\text{Mass energy density}) \times (\text{Oxidized anode density}) \quad (9)$$

The theoretical mass and volumetric energy densities[21] of ZABs are 1218 W h kg^{-1} and 6136 W h L^{-1}, respectively.

Table 1 A comprehensive comparison of ZAB performance based on INMFs as the air-electrode

Samples	OCP[a] (V)	MPD[b] (mW cm^{-2})	RTO[c] (V)	SC[d] (mA h g_{Zn}^{-1})	ED[e] (W h kg_{Zn}^{-1})	ZUR[f] (%)	Stability (hours)	Ref.
$Co_3FeS_{1.5}(OH)_6$	—[g]	113.1	0.84@2 mA cm^{-2}	898@20 mA cm^{-2}	—	109.5	36	48
MnO/Co/PGC	1.52	172	0.85@1 0 mA cm^{-2}	873@5 mA cm^{-2}	1056	106.5	—	49
Co-SAs@NC	1.46	105.3	0.7 V@2 mA cm^{-2}	897.1@20 mA cm^{-2}	—	109.4	16.67	50
Pd/FeCo	1.42	117	~0.88 V@10 mA cm^{-2}	821@10 mA cm^{-2}	854	104.1	200	51
SA-PtCoF	—	130	0.9 V@10 mA cm^{-2}	816.3@30 mA cm^{-2}	798.3	99.5	100	19
N,P/CoS_2@TiO_2 NPFs	—	—	~0.8 V@10 mA cm^{-2}	610@10 mA cm^{-2} 580@50 mA cm^{-2}	—	74.4 70.7	133	94
NiS_x FHF	—	—	1 V@2 mA cm^{-2}	—	—	—	~50	95
CoS_x@PCN/rGO	1.38	—	~1.25 V@50 mA	—	—	—	43.8	96
CoNi@NCNT/NF	1.40	127	~0.8 V@5 mA cm^{-2}	655@5 mA cm^{-2} 631@20 mA cm^{-2}	845 738	79.9 76.9	90	97
MNG-CoFe	~1.5	97.7	~0.5@10 mA cm^{-2}	—	—	—	18	98
SA-PtCoF	1.31	125	~1 V@10 mA cm^{-2}	808@10 mA cm^{-2} 806@20 mA cm^{-2}	785	98.5 98.3	240	38
$Cu_{6.81}$-CoFS	1.44	255	0.5 V@10 mA cm^{-2} 0.93 V@100 mA cm^{-2}	—	—	—	240	39
$Pt_{1.1}$%$Fe_{8.8}$%Ni PF	1.45	175	0.64@20 mA cm^{-2}	816@20 mA cm^{-2} 793@50 mA cm^{-2}	938.4 856.4	99.5 96.7	500	43
PdNiMnO-PF	1.37	211.6	~0.7@10 mA cm^{-2}	812.9@10 mA cm^{-2}	958	99.1	2000	54

[a] OCP: open-circuit potential. [b] MPD: maximum power density. [c] RTO: round-trip overpotentials. [d] SC: specific capacity. [e] ED: energy density. [f] ZUR: Zn utilization ratio. [g] —: values not given in the work.

2.5. Rate performance of ZABs

Generally, the rate performance of ZABs is evaluated by measuring the output cell voltage or discharge curves at various current densities[43,54] (for example, from 1 to 100 mA cm^{-2}). Each current density is held for at least 1 hour to obtain steady-state conditions. The higher the output cell voltage at the same current density, the better the performance of a ZAB.

2.6. Long-term stability and battery failure time of ZABs

The long-term stability of ZABs is usually assessed by continuous charge/discharge cycling tests, the test times of more than 500 hours are recommended with a relatively high charge/discharge current density[43,54,59] (for example, 10 mA cm^{-2}). And the round-trip overpotentials of ZABs before and after long-term stability are compared to check the rechargeability and durability.[60–65] Undoubtedly the smaller round-trip overpotentials between the initial conditions and after the test, the better the long-term stability of ZABs. The failure time of ZABs is primarily determined by the Zn anode, rather than the air cathode. In particular, passivation, shape change, dendritic growth, and hydrogen evolution in the aqueous alkaline electrolyte are currently the most critical factors affecting the cycle lifetime of the ZABs.[21,66]

2.7. Evaluation of self-standing INMFs toward ZABs

The evaluation of self-standing INMFs for use in ZABs is different from traditional powder catalysts that are supported on conductive substrates, where the active phases and loading of catalysts can be easily calculated.[67] In contrast, the precise loading of self-standing INMFs is difficult to determine because only a thin film on the surface of INMFs acts as the real active phase.[3,43,54,68] Therefore, the performance of ZABs using self-standing INMFs should be evaluated more carefully. Additionally, carbon paper or cloth is necessary to act as a gas diffusion layer to avoid the issues of water flooding and electrolyte leaking from air electrodes.[19,38,69]

3. Self-standing INMF air-electrode

3.1. The advantages of self-standing INMFs

In this review, we mainly focus on the self-standing INMFs prepared by electrodeposition with an anodization post-treatment, as well as magnetron sputtering methods. The common regulatory strategies are shown in Fig. 5. Compared to traditional powder materials, self-standing INMFs have many advantages as cathodes for ZABs.[11,17] For example, when using traditional powder materials such as Pt/C, IrO_2, and RuO_2 as air cathodes for ZABs, a binder such as Nafion and PFTE solutions are usually needed to help the powder materials attach firmly to the surface of

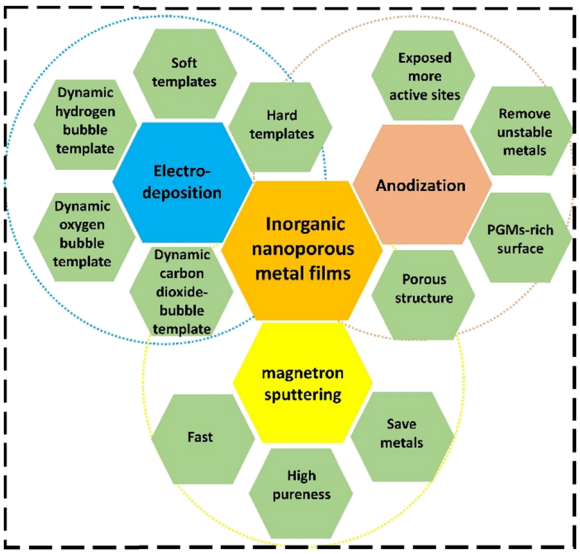

Fig. 5 Methods to prepare INMFs and the common regulatory strategies.

the conductive substrates (such as carbon paper, carbon cloth, metal foams, *etc.*).[15,70–72] This process results in several problems, such as the use of carbon paper/cloth with a porous structure not only increasing the cost of the ZABs system but also causing carbon corrosion under high potential/current density.[21] Other metal-based substrates such as Ni, Co, and Ti may lack porosity, thus limiting the gas diffusion and mass transfer during ZAB operation.[27] The use of binders may block the active sites of the catalysts, increase the thickness and interface resistance of the catalytic layer, and hinder mass/ion transport during the reaction.[28,29] The above-mentioned disadvantages of powder materials result in poor ZABs performance with low PGM utilization, quick performance decay, and high system costs for developing ZABs.[18]

Self-standing INMFs are a more attractive alternative to traditional air electrodes due to their high PGM utilization efficiency of PGMs, anti-corrosive and stable properties under harsh conditions, and large surface area with numerous active sites and pore channels. These materials offer benefits such as facilitating mass transport, high accessibility to the catalytically active metal surface,[17,18,73] and the ability to relax mechanical strain caused by volume change. Additionally, their additive-free nature allows for cost-effective fabrication without the need for binders or conductive substrates. Most self-standing INMFs are PGM-free or contain only small amounts, yet remain highly active and stable, reducing dependence on precious metals and saving costs. Overall, the three-dimensional open channels and high surface area of self-standing INMFs make them ideal for use in ZABs.

3.2. Low-Pt-based self-standing INMFs

The performance of ZABs is mainly dependent on the activity of the air electrode since the same reaction of Zn foil/plate is used at the anode side, with a fast 2e reaction process (eqn (1)). It is reported that Zn-based alloys with three-dimensional structures can be adopted for dendrite-free and high performance of ZABs.[19,20] However, the cathode side includes both the ORR and OER processes during the discharge and charge process, both of which are 4e reactions with sluggish kinetic rates. Thus, most of the current studies focus on developing high-efficiency bifunctional air electrodes. The conventional air electrodes were composed of Pt/C and IrO_2/RuO_2 for the ORR and OER, respectively. These powder PGM-based catalysts show gentle catalytic activity for ZABs. However, their scarcity, high cost, and high loading largely hinder the large-scale commercialization of ZABs. Additionally, when using these powder materials as an air electrode, a binder or additive (such as Nafion and PTFE solutions) is usually needed to support the powder catalysts on conductive substrates (such as carbon paper, carbon cloth, titanium/nickel foam, *etc.*). These may block the active sites of the catalysts, increase the thickness and interface resistance of the catalytic layer, and hinder mass/ion transport during the reaction. The above-mentioned disadvantages of powder materials result in poor ZAB performance with low PGM utilization, quick performance decay, and high system costs for developing ZABs. Thus, it is urgent to develop alternative materials for air electrodes with high PGM utilization efficiency, anti-corrosive and stable properties under harsh conditions, and a high surface area with plenty of available active sites, pore channels, and self-standing structures.

In recent years, a series of efforts have been made by our group to develop INMFs with unique physicochemical properties.[74–76] These INMFs can be widely used as highly-efficient electrode materials in water splitting,[68,77–86] supercapacitors,[87–90] lithium-ion batteries,[3,91] aluminum-ion batteries,[92] magnesium-ion batteries,[6] fuel cells,[41,93] and high-performance air electrodes in ZABs.[38,39,43,51,94–99] In this section, we will summarize the recent progress of INMFs as self-standing air electrodes with low/non-PGM loading for rechargeable ZABs. The structure–composition–performance relationship between INMFS and ZABs will be discussed in-depth.

3.2.1. Low Pt loading of INMFs mediated by a dynamic oxygen-bubble template (DOBT). The air electrode with low PGM loading and high PGM utilization efficiency is desired for ZABs, while a different crystal facet shows different catalytic activity. For example, the activity of Pt(*hkl*) in an alkaline solution for the oxygen reduction reaction (ORR) decreases in the order of (100) < (110) < (111) due to the structural sensitivity of OH adsorption and its impact on ORR kinetics.[100] The electrochemical deposition coupled with electrochemical anodic oxidation provides an ideal way to control the exposed crystal facet.[18] The production of porous films (PFs) can be achieved through top-down etching or bottom-up deposition processes. One such process is the dynamic hydrogen bubble template (DHBT) technology,[101] which is considered a green and simple method for creating metallic PFs. In DHBT, hydrogen (H_2) bubbles form *in situ* and act as pore-forming agents through water electrolysis. However, the intense H_2 bubbles produced by the cathodic hydrogen evolution reaction (HER) make it difficult to maintain stable adsorption/desorption equilibrium during the electrodeposition process, leading to disordered and uneven microporous structures. Additionally, the DHBT process requires precise control of the applied voltage to balance the competition between the HER and metal ion electrodeposition, but this becomes complicated when trying to create porous alloy films, due to the different reduction potentials of metal ions and the varying crystal structures and nucleation-growth modes of the metals. As a result, creating uniform and homogeneous porous alloy films through the DHBT method is challenging. Based on DHBT, a technique proposed by our group is to integrate bottom-up electrodeposition and top-down anodization processes to create PtNi porous films (PFs) that exhibit a high degree of exposure of the Pt active sites. A square-wave potential was employed to control the dynamic oxygen-bubble template (DOBT) programmatically (Fig. 6a), thereby adjusting the morphology of the catalyst and uncovering active facets of Pt in PtNi PFs.

To understand the formation mechanism of nanopores and the ability to manipulate the porous structure of PtNi PFs, the proposed DOBT-directed anodization was performed using square-wave voltages of varying magnitudes, including upper voltages (E_u) of 1.5 V, 1.7 V, and 2.2 V, all with a constant amplitude of 1.3 V. The Pt content in the PtNi PFs is extremely

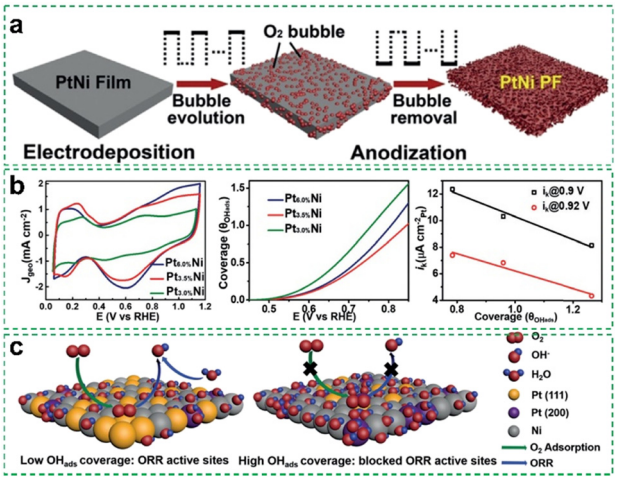

Fig. 6 (a) An illustration of the process for fabricating PtNi PFs using DOBT. (b) The CV curves, reversible OH_{ads} coverage, and the specific kinetic current densities of different samples at different potentials. (c) The illustration depicts the ORR process on low and high OH_{ads} coverage. Adapted with permission from ref. 99 Copyright 2019, Wiley-VCH GmbH.

low and decreases as the voltage increases, with $Pt_{6.0\%}Ni$, $Pt_{3.5\%}Ni$, and $Pt_{3.0\%}Ni$ having 6.0 at%, 3.5 at%, and 3.0 at% Pt, respectively, when the applied voltage is 1.5 V, 1.7 V, and 2.2 V. The SEM and TEM results show that the composition and pore structure of the PF materials is highly influenced by the applied voltage. The $Pt_{6.0\%}Ni$ PF exhibits a mesoporous structure with pores ranging from 20–50 nm due to the generation of O_2 bubbles as an ideal gaseous template. On the other hand, the $Pt_{3.5\%}Ni$ PF displays a highly porous structure with similar pore sizes as the $Pt_{6.0\%}Ni$ PF but a smaller double layer capacitance (C_{DL}) of 2.3 mF cm^{-2} compared to the 2.7 mF cm^{-2} of the $Pt_{6.0\%}Ni$ PF. This reduction in the double-layer capacitance can be attributed to the higher anodic voltage used in the $Pt_{3.5\%}Ni$ PF, which results in an increased generation rate of O_2 bubbles and slight bubble aggregation. While further raising the applied E_u to 2.2 V results in a $Pt_{3.0\%}Ni$ with a disordered porous structure and decreased C_{DL} of 0.4 mF cm^{-2}. At a high anodic potential, the generation of O_2 bubbles is intense and they quickly come together to form large bubbles. Additionally, a higher voltage leads to a greater amount of OH* coverage on the oxidized Ni surface, resulting in a hydrophilic surface that facilitates the release of O_2 bubbles. This disrupts the balance of periodic O_2 adsorption and desorption, causing the synthesis directed by DOBT to fail and preventing the formation of a nanoporous structure at high anodic voltage.

The anodization process directed by DOBT results in a well-controlled nanoporous structure and selective exposure of Pt facets in the PtNi PFs. Two sets of lattice fringes with lattice spacings of 0.21 nm and 0.19 nm, corresponding to face-centered cubic (fcc) Pt(111) and (200) facets, respectively, are found on all three samples. However, the $Pt_{3.5\%}Ni$ PF shows enrichment of Pt(111) facets. While the $Pt_{6.0\%}Ni$ and $Pt_{3.0\%}Ni$ PFs display a uniform distribution of these facets, indicating that the exposure of specific Pt facets can be controlled by adjusting the voltage applied during the anodic process. The optimum sample $Pt_{3.5\%}Ni$ PF shows outstanding ORR activity due to the priority exposed active crystal (111) facet. An ORR half-wave potential ($E_{1/2}$) of 0.80 V_{RHE} was obtained on $Pt_{3.5\%}Ni$ PF, together with an electron transfer number of 3.9 and hydrogen peroxide yield (H_2O_2) below 5%. In contrast, an inferior ORR performance was found on $Pt_{6.0\%}Ni$ PF and $Pt_{3.0\%}Ni$ PF. The ORR activities of PtNi PFs are influenced by their structure due to the structure-sensitive adsorption of OH_{ads} on Pt(*hkl*) (Fig. 6b), which impacts the ORR kinetics and modifies the reaction mechanism as it hinders the adsorption and transfer of electrons in O_2 (Fig. 6c). It is found that the OH_{ads} coverage (ΘOH_{ads}) on $Pt_{3.5\%}Ni$ PF is much lower than on $Pt_{6.0\%}Ni$ PF and $Pt_{3.0\%}Ni$ PF (Fig. 6b) due to the OH_{ads} affinity on Pt(111) being much lower than Pt(200). Thus, the DOBT provides an efficient method to control the crystal facet of the materials, which can be used to study the composition-structure-performance relationship and screen the optimized catalysts quickly.

3.2.2. Low Pt loading of INMFs mediated by a dynamic carbon dioxide-bubble template (DCBT). DHBT and DOBT can be used to synthesize self-standing, conducting INMFs. However, the reaction of these two strategies, HER and OER are still too quick to control the generation, adsorption, residing, and desorption of H_2/O_2 bubbles on the surface of INMFs. Inspired by these two strategies, our group further developed a dynamic CO_2-bubble template (DCBT) approach to fabricate PtFeNi porous films (PFN PFs). In this DCBT approach, the generation of CO_2 bubbles as gas-phase templates was achieved through methanol electrooxidation. The behavior of CO_2 bubbles on the surface of PFN alloys, including adsorption, residing, and desorption, was studied and controlled by adjusting the frequency of the applied triangular-wave voltage. This allowed for regulation of the surface morphology and Pt exposure of PFN PFs by adjusting the coverage of CO_2 bubbles on the surface.

The use of triangular-wave voltage is crucial to produce PFN PFs with a uniform nanoporous structure and optimally exposed Pt active sites (Fig. 7a and b). It is known that the surface of Pt is poisoned easily by CO adsorption (CO_{ads}). To tackle the surface poisoning issue of Pt caused by CO_{ads}, the use of triangular-wave voltage can establish a steady-state equilibrium of CO_2 bubble generation and detachment on the PFN films (Fig. 7b). This approach enabled the implementation of DCBT-directed synthesis. The triangular-wave voltage mode applies a symmetrical linear ramp waveform to the surface, with a constant frequency and a given voltage amplitude, like the voltage control mode used in cyclic voltammetry (CV). In contrast, using square-wave anodization voltages results in methanol molecules being first absorbed onto the Pt surface, followed by dehydrogenation to form CO_{ads} as depicted in Fig. 7a. However, this strong adsorption of CO_{ads} onto the Pt surface poisons the Pt active sites, decreasing their activity for MOR and preventing the full MOR process to CO_2.

The DCBT-directed synthesis was conducted in an acidic electrolyte involving the electrochemical oxidation of the surface nickel, which is then dissolved by H^+. If CO_2 bubbles are produced and cover the oxidized nickel surface, it reduces the etching rate of the PFN film as it obstructs the direct contact between the oxidized nickel and H^+. By switching the applied

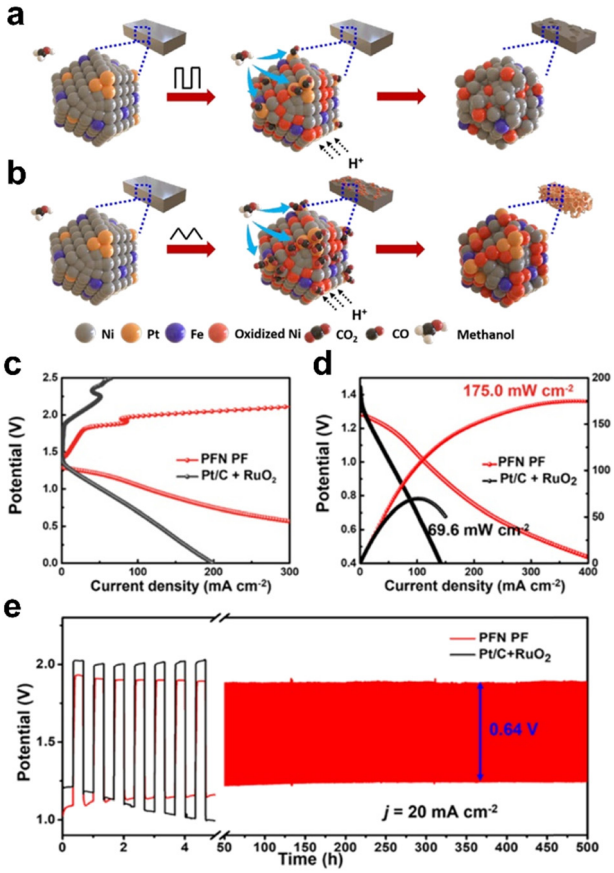

Fig. 7 A schematic illustration of DCBT-directed synthesis utilizing (a) square-wave voltage and (b) triangular-wave voltage. (c) Charge/discharge polarization curves, (d) power density curves, and (e) stability for ZABs with $Pt_{1.1\%}Fe_{8.8\%}Ni$ PF and Pt/C + RuO_2 as the air-electrode at a current density of 20 mA cm^{-2}. Adapted with permission from ref. 43 Copyright 2021, ACS Publications.

triangular-wave voltages to a potential range without CO_2 production, the adsorbed CO_2 bubbles can quickly detach from the PFN surface, allowing for fine-tuned microstructures. The MOR occurs on Pt-rich sites in the PFN film, producing CO_2 bubbles and protecting the Pt from over-etching, preserving the active sites. The dynamic control of CO_2 bubble adsorption and desorption through triangular-wave voltage anodization allows for the successful fabrication of PFN PFs with a highly ordered nanoporous structure and exposed Pt active sites.

In the DCBT-directed process, the microstructure of the PFN film, specifically the pore size, and distribution, is primarily influenced by the coverage of CO_2 bubbles on its surface. This coverage is dependent on several factors, including the gas generation rate, the time the bubbles spend on the electrode surface, and the rate at which they grow to the point of detachment. As all these processes are time-sensitive, adjusting the frequency of the triangular-wave voltage can be an effective way to control the bubble coverage on the PFN film surface and therefore fine-tune the microstructure. As a result, three different frequencies were selected and the obtained INMFs are $Pt_{0.9\%}Fe_{9.0\%}Ni$ (at 10 mHz), $Pt_{1.1\%}Fe_{8.8\%}Ni$ (at 100 mHz), and $Pt_{0.7\%}Fe_{8.1\%}Ni$ (at 1 Hz), respectively. It was found that the optimum sample $Pt_{1.1\%}Fe_{8.8\%}Ni$ (at 100 mHz) has a homogeneous nanoporous and much higher C_{DL} compared to the other control samples. Thus, it demonstrates a significantly improved performance in terms of the ORR and OER, with an $E_{1/2}$ of 0.87 V_{RHE} for the ORR and an overpotential of 288 mV at a current density of 10 mA cm^{-2} for the OER. The excellent ORR and OER performance can be attributed to the abundant Pt active sites that are exposed and the Fe-doping, which served as the real active sites, respectively.

The performance of the PNF PFs as an air-electrode is excellent, as evidenced by their outstanding ZAB results. An OCP of 1.45 V was found, and the charge/discharge gap of PNF PFs is much smaller than commercial Pt/C + RuO_2 (Fig. 7c). The maximum power density is 175 mW cm^{-2} on the PNF PFs air-electrode (Fig. 7d), which is 2.5 times that of Pt/C + RuO_2. After conducting long cycling tests over 500 hours, no significant degradation in performance was detected (Fig. 7e). This highlights the exceptional stability and durability of PNF PFs, which can withstand 750 cycles without showing any apparent performance decay (Fig. 7e). The PNF PFs air-electrode also shows a good rate performance under a high current density. The specific capacities were 816 mA h g^{-1} and 793 mA h g^{-1} at discharge current densities of 20 mA cm^{-2} and 50 mA cm^{-2}, respectively for the PFN PFs. This equates to energy densities of 938.4 W h kg^{-1} and 856.4 W h kg^{-1} and ZURs of 99.5% and 96.7% respectively. Thus, the DCBT method has proven to be an effective way to produce high-performing air electrodes for ZABs.

3.2.3. Low Pt loading of INMFs by trapping interstitial F atoms. Despite their favorable surface electronic structures for electrochemical reactions, PGMs, including Pt, Ru, and Ir-based materials, are still primarily used as ORR/OER electrocatalysts. However, their high cost and scarcity hinder their widespread usage in ZABs. One efficient way to maximize the utilization, such as Pt, is to reduce the size to the atom level. Due to the high number of active sites produced by the low coordination and unsaturated chemical environment, these atomic Pt catalysts exhibit a higher level of catalytic activity than commercial Pt nanoparticles. However, the weak interaction between the Pt atom and conducting support/substrate results in the poor stability of materials. Recently, our group reported a new approach that combines bottom-up electrodeposition and top-down fluorine-plasma (F-plasma) etching to stabilize atomic Pt in PtCo nanosheets (Fig. 8a).[38] The presence of interstitial F atoms in the PtCo alloy (PtCoF) causes lattice distortion, which is crucial in maintaining the stability of atomic Pt on the surface of the PtCoF (SA-PtCoF), and it is achieved by equalizing the surface free energy. Due to the self-standing and additive-free characteristic of SA-PtCoF, it has abundant active sites and a high surface area.

The SA-PtCoF catalyst has been found to exhibit bifunctional ORR/OER capabilities and has outperformed commercial Pt/C@RuO_2 catalysts. It is found that atomic Pt, stabilized in the PtCoF matrix with low coordination and an unsaturated configuration, plays an important role as the active site in enhancing the ORR activity. On the other hand, the electron-donating Co in SA-PtCoF serves as an active site for the OER. The onset potentials for the ORR and OER were 0.95 V_{RHE} and 1.50 V_{RHE}, respectively.

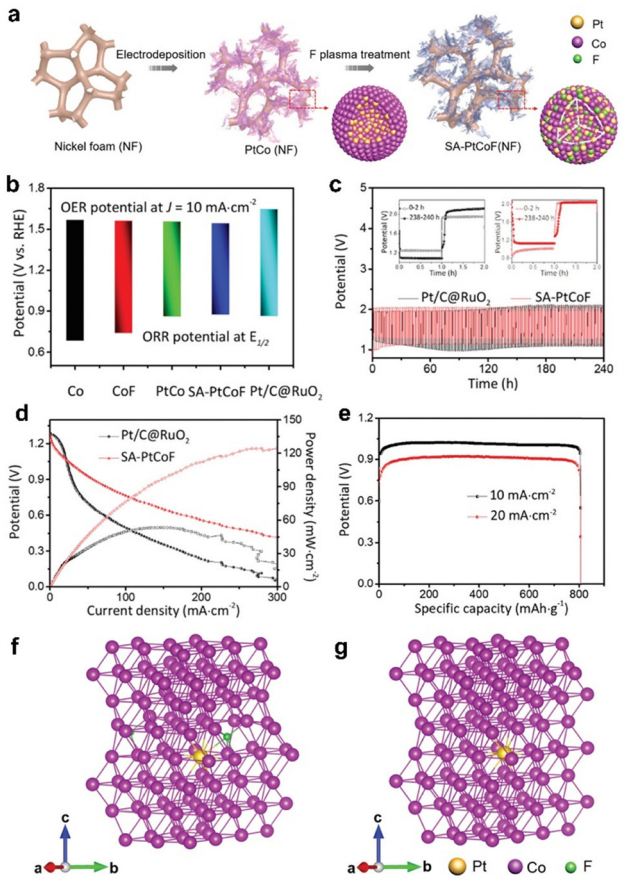

Fig. 8 (a) The process of fabricating SA-PtCoF nanosheets. (b) Overall bifunctional ORR/OER performances on SA-PtCoF and control samples. (c) The long-term discharge/charge curves of SA-PtCoF and Pt/C@RuO_2. The first and last discharge/charge profiles are shown in the inset. (d) The ZABs polarization curves of SA-PtCoF and Pt/C@RuO_2. (e) The long-term discharge curves of the ZABs using the SA-PtCoF cathode at current densities of 10 and 20 mA cm^{-2}. DFT computational study of structural changes between (f) PtCoF and (g) PtCo. Adapted with permission from ref. 38 Copyright 2020, Royal Society of Chemistry.

The bifunctional activity of SA-PtCoF was further evaluated by calculating the potential difference between the $E_{1/2}$ for the ORR and the potential at 10 mA cm^{-2} for the OER. The SA-PtCoF catalyst demonstrated a superior minimal potential difference of 658 mV, compared to the control samples (Fig. 8b). Hence, the SA-PtCoF is an ideal candidate for air electrodes in ZABs. The galvanostatic charge/discharge profile was recorded for SA-PtCoF and Pt/C@RuO_2 (Fig. 8c). In comparison to Pt/C@RuO_2, SA-PtCoF exhibits a smaller voltage gap during charge/discharge cycles. After cycling for 240 hours, the voltage gap for SA-PtCoF decreases significantly from 1.03 V to 0.9 V, indicating an activation process during cycling. In contrast, the commercial Pt/C@RuO_2 electrodes show an increased voltage gap from 0.69 V to 1.03 V, which suggests degradation of the catalyst. Besides, SA-PtCoF also exhibits a maximal power density of 125 mW cm^{-2} at 266 mA cm^{-2} (Fig. 8d), *ca.* 2.3 times than those of commercial Pt/C@RuO_2 (55 mW cm^{-2}). The SA-PtCoF was determined to have a specific capacity of 808 mA h g^{-1} at a current density of 10 mA cm^{-2} and 806 mA h g^{-1} at a current density of 20 mA cm^{-2} (Fig. 8e), resulting in ZUR values of 98.5% and 98.3% respectively. The exceptional performance of ZABs can be attributed to the interaction between the catalyst and support, as well as the synergistic effects between the atomic Pt and the alloyed PtCoF matrix. This work presents a novel approach to stabilize atomic Pt on alloyed PtCoF nanosheets through the incorporation of interstitial F atoms. The trapped F atoms cause lattice distortion in the PtCoF matrix, reducing the strength of the Pt–Co bond, thereby stabilizing the surface Pt single atoms, and improving the utilization efficiency of Pt in rechargeable ZABs.

Density functional theory (DFT) calculations were performed to investigate the influence of F atoms on PtCo in SA-PtCoF nanosheets. It was found that the lattice parameters of the nearest neighbor distance between the Pt atom and its Co atoms increased from 2.49 Å to an average of 2.59 Å after the F atom was inserted (Fig. 8f–g), resulting from an anisotropic distortion near the Pt atom. Furthermore, the vibrational frequencies decreased when the F atom was inserted, indicating weakening of the Pt bond to its neighboring Co atoms. Therefore, interstitial F atoms play an important role in weakening the Co–Pt bond and contributing to free Pt atoms on the surface of nanosheets with low energy barriers.

3.2.4. Low Pt loading of Pt–CoO networks. In some cases, the increased Pt-specific activity for the ORR was due to the low electrochemically active surface area (ECSA),[102–104] which is only suitable for the region controlled by kinetics. However, at higher overpotentials in real systems, the low ECSA leads to limitations as mass transport limits the reaction, rather than being limited by kinetics. Therefore, there is an urgent need to develop self-supported INMFs with high ECSA to promote the commercialization of ZABs and fuel cells.[40,42,105,106]

Recently, Gustav W. Sievers *et al.*[73] reported self-supported Pt–CoO networks with a high surface area and high specific activity for the ORR. The nanoporous Pt–CoO networks were prepared using alternating magnetron sputtering of Co and Pt layers, followed by acid leaching of the non-noble CoO component. Compared to conventional wet-chemical approaches, the magnetron sputtering technique can be easily scaled up on different substrates, such as glassy carbon, and carbon paper, can be used. This self-standing Pt–CoO network does not require any carbon support material, which can avoid the potential carbon-corrosion problems of standard carbon-supported catalysts.[107] By changing the Pt:Co starting compositions, samples with different Pt:Co at% can be obtained. As shown in Fig. 9a, the optimized Pt–CoO shows a porous structure with elemental distribution at the nanometre scale. The ECSA of Pt–CoO was found to be as high as 156 m^2 g_{Pt}^{-1}, which is much higher than other benchmark Pt and Pt_3Co catalysts (Fig. 9b). The mass activity of Pt–CoO at 0.9 V_{RHE} is as high as 8.37 A g_{Pt}^{-1}, which is approximately eight times higher than state-of-the-art supported Pt/C catalysts (Fig. 9c). The high catalytic activity can be attributed to the optimized binding energy of the catalyst surface with the reaction intermediates O, OH and OOH. Additionally, alloying Pt with Co can change the electronic structure of Pt and improve its ORR performance. This work

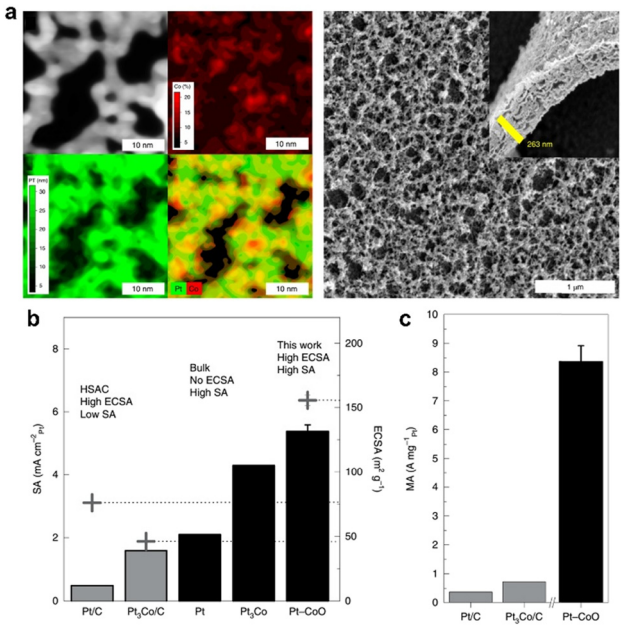

Fig. 9 (a) High-angle annular dark-field (HAADF) scanning transmission electron microscopy (STEM) and scanning electron microscopy (SEM) images of self-supported nanoporous Pt–CoO networks. (b) ORR-specific activity (SA) and ECSA of Pt–CoO and other control samples. (c) ORR mass activity (MA) of Pt–CoO and other control samples. Adapted with permission from ref. 73 Copyright 2021, Springer Nature.

provides a new approach to developing a nanoporous catalyst with high ECSA and activity for the ORR without support materials, which is industrially scalable and will inspire the development of ZABs and fuel cells.

3.3. Low-Pd-based self-standing INMFs

Pt-based materials have been widely studied for the electrocatalytic reaction,[5,44,45,108–115] especially as a benchmark catalyst for the ORR due to their favorable surface electronic structures that support electrochemical reactions.[93] Despite their outstanding performance, the high cost and scarcity of Pt hinder its widespread use in ZABs.[15] An alternative material to consider is palladium (Pd), which exhibits a comparable level of electrocatalytic activity to Pt in alkaline environments, yet it has a much higher abundance in the earth's crust.[4,41,46,51,54,116–123] Herein, some representative studies on Pd-based self-standing INMFs will be discussed in the following.

3.3.1. Low-Pd-based INMFs with a strong metal–support interaction. Conventional carbon-supported catalysts, such as Pt/C and Pd/C, were found to have a weak metal–support interaction.[116] This weak interaction between the metal and the support results in restricted mass and electron transfer, which hinders the electrocatalytic reaction.[124] To overcome this issue, a strong interaction between the catalyst and the functional support is necessary. Based on this, recently, our group reported PdNiMnO porous films (PFs) with ultra-low Pd loading as a bifunctional air electrode for ZABs. This PdNiMnO film was surface oxygenated to enhance the interaction between the Pd and support interfaces, thereby improving the utilization efficiency of Pd (Fig. 10a). Mn doping was introduced to promote surface oxygenation through a simple anodization process, which created well-exposed interfaces between Pd and the support, thus strengthening the strong metal–support interaction (SMSI) effects and improving the ORR performance. Pd with a regulated electronic structure and optimized adsorption and cleavage energy for O_2 serves as real active sites for the ORR. Meanwhile, the Ni-containing oxygenated catalyst acts as both an active component for the OER and functional support for stabilizing Pd, making the PdNiMnO a dual-functional catalyst for zinc–air flow batteries (ZAFBs, Fig. 10b). According to the DFT calculations, the sublayer of Pd(111) surfaces is the preferred location for Mn doping as compared to the outermost layer. The free energy changes for all the ORR elementary steps on Mn–Pd(111) became negative under a potential of 0.71 V, which is higher than undoped Pd(111). The DFT result suggests that Mn doping enhances the ORR activity of Pd(111) by weakening the interaction between Pd and ORR intermediates. Additionally, the enthalpy change of a Pd atom from the outermost layer of Mn–Pd(111) is much higher than that of undoped Pd(111), indicating that the sublayer Mn can also stabilize the outermost surface of Pd atoms. Therefore, the PdNiMnO PFs exhibit increased activity and stability for ORR, OER, and ZAB performances.

The OCP of the ZAFB that uses PdNiMnO PFs as the self-standing air-electrode was 1.37 V, and a maximum power density of 211.6 mW cm^2 (Fig. 8c) can be delivered.

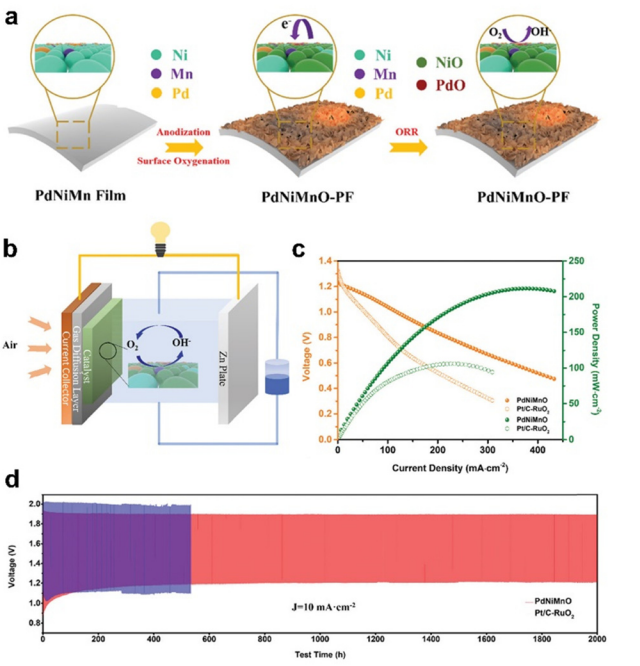

Fig. 10 (a) Schematic illustration depicting the process of surface oxygenation of the PdNiMnO PFs catalyst. (b) The schematic illustration depicts the operating principle of an aqueous zinc–air flow battery. (c) A comparison of polarization and power density curves for PdNiMnO PFs and Pt/C-RuO_2. (d) The long-term discharge/charge curves of the ZABs using the PdNiMnO PFs and Pt/C-RuO_2 cathode. Adapted with permission from ref. 54 Copyright 2022, Royal Society of Chemistry.

Furthermore, the ZAFB (PdNiMnO) displayed an impressive specific capacity of 812.9 mA h g^{-1} and an energy density of 958 W h kg^{-1}, leading to a ZUR of 99.1%. A remarkable stability for cycling was observed, with a duration of over 2000 hours and a minimum voltage gap of 0.69 V at a current density of 10 mA cm^{-2} (Fig. 10d). The superb activity and stability were achieved through enhanced interaction between the Pd support and a tailored electronic structure of Pd. Thus, it provides an efficient method to prepare a robust air-electrode by strengthening the interaction between the active metal and the support.

3.3.2. Self-standing FeCo glassy alloy supported Pd. The robust and corrosion-resistant support is anticipated to replace conventional carbon supports. Our group recently reported that a self-standing FeCo glassy alloy can be utilized as an effective support.[51] The conductive skeleton of the porous glassy alloy is used to stabilize cocatalysts for oxygen reduction, where FeCo acts as the primary active phase for the OER. To demonstrate the effectiveness of this catalytic support, ultrasmall Pd nanoparticles are anchored onto the porous FeCo as active sites for the ORR, resulting in the Pd/FeCo structure for ZABs. The Pd/FeCo electrocatalyst shows significantly improved activity for both the ORR and OER in alkaline media. It has an $E_{1/2}$ of 0.85 V for the ORR and a potential of 1.55 V to reach 10 mA cm^{-2} for the OER. When used in a ZAB system (Fig. 11), the Pd/FeCo electrocatalyst delivers an output power density of 117 mW cm^{-2} and demonstrates excellent cycling stability for over 200 hours (400 cycles).

3.4. PGM-free self-standing INMFs

Despite the significant advances made in PGM-based materials such as air electrodes for ZABs, to reduce costs and increase commercial applications, it would be a wise decision to develop PGM-free air electrodes with equal or higher activity and stability.[16,125] Strain control, doping, and innovative surface structural engineering have been proven to be effective techniques in the creation of high-performance PGM-free air electrodes.

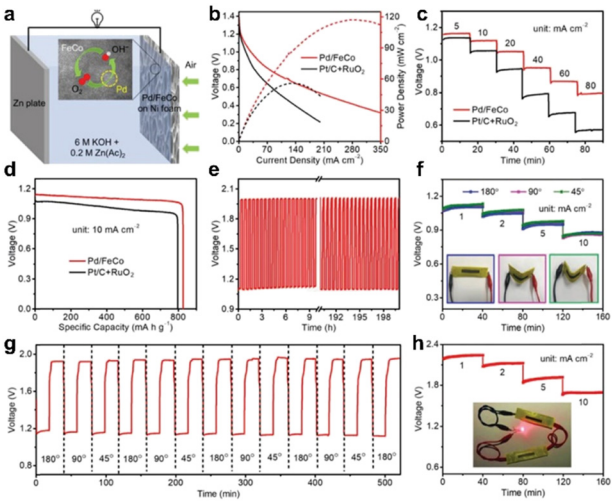

Fig. 11 (a) A schematic illustration depicting the operating principle of ZABs. (b) Polarization and power density curves, (c) discharge curves at different current densities, and (d) specific capacity measurements. (e) The galvanostatic discharge–charge cycling performance of the Pd/FeCo-based ZABs. (f) The discharge curves of the Pd/FeCo-based flexible solid-state ZAB under different bending conditions. (g) The galvanostatic discharge–charge cycling performance of the Pd/FeCo-based solid-state ZABs. (h) The discharge curves of tandem Pd/FeCo-based solid-state ZABs. Adapted with permission from ref. 51 Copyright 2020, Wiley-VCH GmbH.

3.4.1. Strain control of PGM-free INMFs. The efficiency of electrocatalysts for ZABs can be effectively regulated by changes in the local atomic arrangement of a crystal, induced by lattice-mismatch strain. This is primarily due to the modulation of electronic structure configurations, which impact the adsorption energies of oxygen intermediates formed during the ORR and OER. However, the use of strain engineering in electrocatalysis has been limited by the strain relaxation resulting from structural instability, such as dissolution and destruction, leading to inadequate durability in the face of the ORR/OER. Recently, our group reported a new doping strategy aimed at modulating the phase transition and self-supported formation of cobalt fluoride-sulfide (CoFS) nanoporous films using a small amount of copper (Cu) as a dopant.

The synthesis of Cu-CoFS nanoporous films is depicted in Fig. 12a. The process begins with the creation of thin free-standing metallic Co films, which are doped with varying amounts of Cu, through electrodeposition. Then, anodic treatment in a fluorine-containing electrolyte is applied to convert the metallic Cu–Co films into Cu-doped CoF_2 (Cu-CoF_2) nanoporous films. Finally, a sulfurization process is implemented to affect the CoF_2–CoS_2 phase transition, resulting in the formation of nanoporous Cu–CoFS films with a precisely controlled two-phase interface. The well-defined Cu–CoFS heterostructure resolves the issue of structural instability, which helps to establish the relationship between the structure and properties of strained electrocatalysts by revealing the impact of local strain on the electronic structure of the catalyst.

The Cu–CoFS electrocatalyst demonstrates superior onset potentials of 0.91 and 1.49 V_{RHE} for the ORR and OER respectively (Fig. 12b). The Cu–CoFS catalyst also demonstrates excellent charge/discharge cycling performance with a low voltage gap of 0.5 V at a current density of 10 mA cm^2 and 0.93 V at a high current density of 100 mA cm^2, which can operate for more than 240 hours (Fig. 12c) and delivering an outstanding peak power density of 255 mW cm^{-2} (Fig. 12d). In addition, the bend test was conducted on the foldable ZABs and there was virtually no alteration in voltage despite various deformations (Fig. 12e).

From DFT calculations, it has been found that the improved and stabilized ORR/OER activities are achieved through the optimization of the adsorption energy of intermediates. Specifically, the *OOH and *OH species prefer to be adsorbed at the top site of Co atoms, and the bond length of Co–O decreases significantly with increasing strain. However, due to the increase in the bond length of Co–S as the lattice strain increases, the adsorption of *O changes from the bridge site to the top site between Co and O. The overall ORR/OER pathway, along with the corresponding free energy diagrams, is presented in Fig. 12f. It is found that the rate-determining step (RDS) was altered due to a transition from compressive strain to

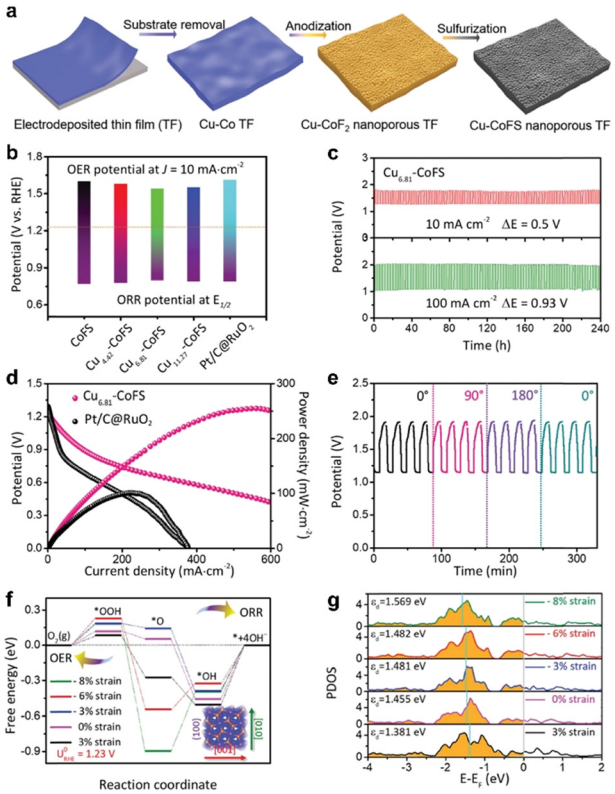

Fig. 12 (a) A diagram illustrating the production process for the nanoporous film made of Cu_x-CoFS is presented. (b) The bifunctional ORR/OER performance. (c) Discharge and charge curves of $Cu_{6.81}$-CoFS in flow cells, with current densities of 10 and 100 mA cm^{-2}, respectively. (d) Polarization curves for both $Cu_{6.81}$-CoFS and Pt/C@RuO_2. (e) Discharge and charge curves of $Cu_{6.81}$-CoFS at different bending angles for foldable ZABs. (f) A free energy diagram for ORR/OER calculated at the equilibrium potential (1.23 V_{RHE}) under different strains. (g) The PDOS is calculated for the d band of Co atoms in the CoS_2(100) facet under various strains. The Fermi level is set to zero, while the d-band center is indicated by the cyan solid line. Adapted with permission from ref. 39 Copyright 2021, Royal Society of Chemistry.

tensile strain. Additionally, as shown in Fig. 12g, an upward shift of the d-band center was observed with increasing lattice strain. This suggests that the adsorption energy of *OOH, *O, and *OH increases with lattice strain, ultimately resulting in a moderate adsorption strength of the intermediates. This study provides new insight into the rational design of efficient electrocatalysts through strain engineering for renewable energy and catalysis.

3.4.2. Innovative structural and heteroatom doping engineering of PGM-free INMFs. We recently reported the preparation of a nickel sulfide (NiS_x) freestanding holey film (FHF) using a combination of bottom-up electrochemical deposition and top-down electrochemical etching strategies followed by sulfuration treatment (Fig. 13a).[95] The porous structure of NiS_x FHF, along with its optimal electrochemically active surface area and active sites, provides exceptional bifunctional electrocatalytic performance for both the ORR and OER. With its porous and freestanding features, NiS_x FHF has great potential as a suitable air-breathing cathode in flexible ZABs, demonstrating stability for over 50 hours during charge/discharge cycling tests.

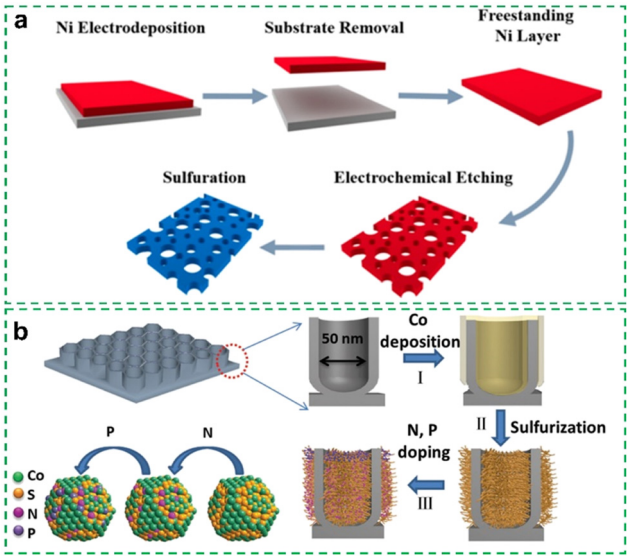

Fig. 13 (a) A diagram illustrating the production process for the NiS_x FHF. Adapted with permission from ref. 95 Copyright 2018, ACS Publication. (b) A fabrication process of the N,P/CoS_2@TiO_2 NPFs. Adapted with permission from ref. 94 Copyright 2018, Wiley-VCH GmbH.

Doping engineering is another efficient strategy to increase the activity and stability of electrocatalysts. Our group reported N,P/CoS_2@TiO_2 nanoporous films (NPFs), synthesized by embedding N,P co-doped CoS_2 nanoclusters inside TiO_2 (Fig. 13b). The activity and stability of N,P/CoS_2@TiO_2 NPFs is enhanced by the N, P dopants, which improve conductivity, increase the active surface area, and facilitate reaction kinetics. The N,P/CoS_2@TiO_2 NPFs exhibit remarkable onset potentials of 0.91 and 1.41 V_{RHE} for the ORR and OER respectively. When used as an air-electrode in ZABs, they demonstrate a decreased charge–discharge voltage difference of 0.8 V at a current density of 10 mA cm^{-2} and exhibit a stable cycling performance over 130 hours. A specific capacity of 610 mA h g^{-1} was acquired, corresponding to a ZUR of 74.4%. The above self-standing PGM-free INMFs provide new approaches for designing highly active and stable air-electrodes for ZABs.

In order to optimize the free energy of adsorption of the ORR and OER intermediates,[13,126–135] it is necessary to regulate the electronic structure of the catalyst through the use of elemental doping with a transition metal or heteroatom. To illustrate, Hu's group[13] utilized Fe-doped Co_3O_4 nanosheets as a binder-free bifunctional cathode for ZABs. The Fe doping allowed for modulation of the electronic structure and enrichment of accessible active sites in the Fe–Co_3O_4 nanosheet, consequently enhancing mass/electron transfer effectively. As a result, the Fe–Co_3O_4 nanosheet demonstrated a maximum power density of 268.6 mW cm^{-2} for ZABs with a narrow charge–discharge gap of 0.75 V at a current density of 2 mA cm^{-2}; moreover, it exhibited stable operation for over 100 h (300 cycles), indicating the potential value in ZAB application.

Guan *et al.*[136] developed an efficient ORR catalyst for ZABs, which is a mesoporous sulfur-doped Fe–N–C (m-FeSNC). In particular, these catalysts achieved an ORR half-wave potential of 0.904 V and a peak power density of ZABs of up to 221 mW cm^{-2}. The use

of a rational polymerization initiator enhances the co-doing of Fe and S, promoting the creation of electrocatalytic activity Fe–N_X sites. Meanwhile, the electronic structure of m-FeSNC is further regulated through Fe and S doping, contributing to the high electrocatalytic activity of the catalyst.

3.4.3. Surface engineering of PGM-free INMFs. Surface engineering has been extensively used to develop high-performance catalysts. We recently reported the fabrication of surface-modified porous carbon nitride composites (PCN) using a top-down approach, followed by the incorporation of graphene and CoSx nanoparticles (Fig. 14a). The resulting CoS_x@PCN/rGO showed improved conductivity and catalytic activity due to its highly porous morphology and abundant exposed active sites, making it ideal for electrocatalytic reactions.[96] The CoS_x@PCN/rGO can serve as a bifunctional electrocatalyst for both the ORR and OER, with a ΔE value (the potential gap between the overpotential at 10 mA cm^{-2} in the OER and the $E_{1/2}$ in the ORR) of just 0.79 V, significantly lower than that of commercial Pt/C (1.10 V) and RuO_2 (1.08 V), as shown in Fig. 14b. The CoS_x@PCN/rGO electrode also demonstrated excellent rechargeability, with 394 discharge/charge cycles over 43.8 hours (Fig. 14c), which is more stable than commercial Pt/C (171 cycles for 19 hours, Fig. 14d). Furthermore, in comparison to Pt/C, the CoS_x@PCN/rGO electrode showed a more stable and narrower potential gap in long-term cycling, indicating its high catalytic activity and robust chemical stability.

Advancements in technology have now made it possible for nitrogen-doped carbon nanotube (NCNT) arrays to efficiently catalyze the ORR. However, their hydrophobic surface and base-growth mode present limitations in practical applications. To overcome this, the concept of an apically dominant mechanism has been demonstrated by precisely encapsulating CoNi nanoparticles (NPs) within the apical domain of NCNT on Ni foam (CoNi@NCNT/NF, Fig. 15a).[97] Density functional theory calculations show that the ORR catalytic performance of CoNi@NCNT/NF is largely attributed to the synergistic contributions from NCNT and the active sites near the CoNi NPs on the NCNT apical domain. When using the CoNi@NCNT/NF as the air-electrode in a ZABs coin cell, a peak power density of 127 mW cm^{-2} was observed at a current density of 200 mA cm^{-2}

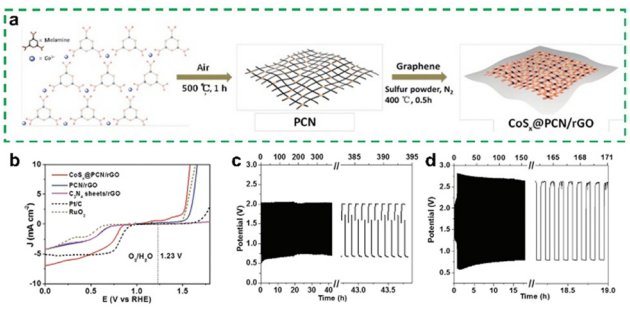

Fig. 14 (a) A diagram illustrating the production process for the COS_x@PCN/RGO. (b) The bifunctional ORR/OER performance of different samples. Cycling curves for rechargeable ZABs at a current of 50 mA for (c) CoS_x@PCN/rGO and (d) Pt/C + RuO_2. Adapted with permission from ref.96 Copyright 2018, Wiley-VCH GmbH.

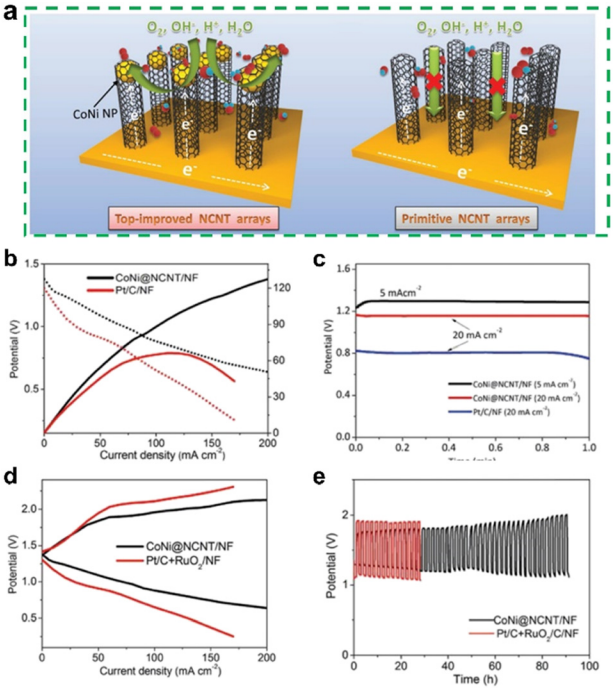

Fig. 15 (a) Schematic illustrating the apically dominant mechanism of CoNi@NCNT/NF. (b) ZAB polarization curves and power density curves. (c) Discharge curves at 5 and 20 mA cm^{-2}. (d) Discharge and charge polarization curves. (e) Cycling curves for rechargeable ZABs at a current of 5 mA cm^{-2} for CoNi@NCNT/NF and Pt/C + RuO2/NF. Adapted with permission from ref. 97 Copyright 2018, Wiley-VCH GmbH.

(Fig. 15b). This is higher than the peak power density of 66 mW cm^{-2} at 115 mA cm^{-2} observed using commercial Pt/C as the air-electrode. The specific capacity of the ZAB coin cell was calculated to be 655 and 631 mA h g^{-1} and at a discharge rate of 5 and 20 mA cm^{-2} (Fig. 15c), resulting in an energy density of 845 and 738 W h kg^{-1}. The corresponding ZUR is 79.9% and 77.0%, respectively. The rechargeability of ZAB using the CoNi@NCNT/NF electrode was further assessed by discharge and charge polarization (Fig. 15d). The stable galvanostatic charge-discharge profiles further demonstrate the robust rechargeability of the ZAB coin cell, as no significant potential drop was observed after long-term cycling of over 90 hours.

4. Conclusions and perspectives

In this review, we have revisited critical descriptors to assess the performance of ZABs and recommend standard testing and reporting methods. Furthermore, we have systematically summarized and discussed the recent progress of INMFs as self-standing air electrodes with low/non-PGMs loading for rechargeable ZABs (Table 1). The relationship between INMFs and ZABs in terms of structure, composition, and performance has been discussed in depth. Despite the significant development of ZABs based on INMFs in recent years, visible challenges and bottlenecks still exist.[137] Therefore, future research should consider the following aspects.

(1) Although electrochemical deposition and anodic oxidation are efficient methods to prepare INMFs, which can reduce system costs and increase active site exposure due to no binder being used, a large amount of metal salt solutions is wasted due to the excessive use of reactants. This particularly concerns the industrial prospects of INMFs toward ZABs, particularly when using PGMs due to their high cost. Therefore, it is necessary and urgent to develop an efficient method to recycle or reuse electrolytes that have reacted, especially those containing PGMs to advance the possible commercialization of self-standing INMFs.

(2) Although electrochemical deposition and anodic oxidation are efficient methods for preparing INMFs, only a limited number of metals/alloys can be prepared by electrochemical deposition. The different deposition conditions, such as thermodynamic equilibrium potentials, need to be considered as a priority due to the significant potential difference between different metal ions to metallic metals. When two metal ions have a similar reduction potential, they tend to form an alloy. However, when there is a large reduction potential difference between two or more metal ions, a core–shell structure, layer structure, or even gradient alloy can be obtained.[3] Therefore, it is recommended to consider the difference in reduction potential when preparing metal or alloy films and it is very important to control the synthesis parameters (such as deposition voltage and time, the concentration of plating electrolyte and reaction temperature, *etc*.).

(3) It is still difficult to synthesize single atomic-based INMFs using the electrochemical deposition and anodic oxidation methods. Since the metal film is generally first prepared, that means a large number of metals need to be used, thus it is difficult to synthesize INMFs under single atom form. While the single atom alloy or doping seems an alternative method to maximize the atomic utilization,[38] especially for the PGMs. The synthesis conditions, for example, the potentials/currents, and reaction times adopted for electrochemical deposition/anodic oxidation should be carefully controlled. The concentration of platting electrolytes also needs to be precisely controlled.

(4) The performance of ZABs, including their activity and stability, still needs improvement. In comparison to H_2-O_2 fuel cells with a fully open system, which has high activity and stability, ZABs with a half-open system need further improvement. For instance, an H_2–O_2 single fuel cell can have a power density of 1–2 W cm^{-2}, which is ten times higher than ZABs with a power density of 100–200 mW cm^{-2} (as shown in Table 1). The faster reaction kinetics of H_2 electrooxidation compared with Zn electrooxidation leads to the higher activity of H_2–O_2 fuel cells compared to ZABs. As a result, the low power density of ZABs limits their application only in small portable devices. Conversely, the high-power density of H_2–O_2 fuel cells allows for a wide range of applications, such as in aviation and automobiles. The fully open system of H_2–O_2 fuel cells permits continuous operation without interruption, whereas for ZABs, even rechargeable ones, the consumption of Zn metal is inevitable, and a fresh Zn metal anode is required periodically to ensure successful operation. These characteristics make ZABs only suitable for use in small portable devices such as hearing aids, although their operating time still needs to be improved.

(5) Although the INMFs show many advantages over powder materials, the hydrophilic/hydrophobic character of different INMFs varies. Generally, INMFs require a hydrophilic character to ensure intimate contact at the gas(O_2)/solid (air-electrode)/liquid (electrolyte) three-phase boundary. However, air electrodes also ask for a hydrophobic character to prevent flooding. Thus, a balance between hydrophilicity and hydrophobicity is important for a good air electrode. While the INMFs can be used as self-standing air electrodes, hydrophobic carbon paper/cloth is often used as an efficient gas-diffusion layer to assist the INMFs. However, the use of carbon paper/cloth not only increases the cost of the ZABs system but also has the problem of carbon corrosion under high potential/current density. Therefore, it is still necessary to address the hydrophilic/hydrophobic issues when preparing INMFs.

(6) The current process of synthesizing INMFs still relies largely on a time-consuming and laborious trial-and-error procedure. Seeking help from computational and theoretical guidance is urgent. Theoretical computation is a powerful tool that can predict efficient catalysts and aid in understanding inherent catalytic mechanisms. Combining experimental and theoretical methods is a more reasonable approach for high throughput, large-scale, and controllable synthesis of INMFs with high activity and stability for ZABs.

Overall, due to the advantages of INMFs, they will be widely used in electrochemical energy storage and transformation devices. The exceptional benefits of safety, high energy density, and affordability make ZABs an environmentally friendly and low-carbon technology for energy storage and conversion. Greater scientific and industrial efforts are encouraged for the advancement of ZABs. Ultimately, ZABs will find applications in numerous fields, including wearable and portable devices.

Author contributions

This work was supervised and conceptualized by Y. Y. J. C. conducted literature research and wrote the original draft. J. C. and Y. Y reviewed and edited the paper.

Conflicts of interest

There are no conflicts to declare.

Acknowledgements

This work was supported by the National Science Foundation under Grant No. CMMI-1851674, CBET-1949840, and ACS PRF (65481-ND10). J. C. acknowledges financial support from the Preeminent Postdoctoral Program (P3) at UCF.

References

1 M. S. Dresselhaus and I. L. Thomas, *Nature*, 2001, **414**, 332–337.
2 B. C. H. Steele and A. Heinzel, *Nature*, 2001, **414**, 224–231.

3 G. Wang, M. Aubin, A. Mehta, H. Tian, J. Chang, A. Kushima, Y. Sohn and Y. Yang, *Adv. Mater.*, 2020, **32**, 2003684.
4 J. Chang, L. Feng, C. Liu, W. Xing and X. Hu, *Angew. Chem., Int. Ed.*, 2014, **53**, 122–126.
5 J. Chang, L. Feng, C. Liu, W. Xing and X. Hu, *Energy Environ. Sci.*, 2014, **7**, 1628–1632.
6 K. Liang, K. Marcus, L. Guo, Z. Li, L. Zhou, Y. Li, S. T. De Oliveira, N. Orlovskaya, Y. H. Sohn and Y. Yang, *Chem. Commun.*, 2017, **53**, 7608–7611.
7 J. E. Trancik, *Nature*, 2014, **507**, 300–302.
8 Z. P. Cano, D. Banham, S. Ye, A. Hintennach, J. Lu, M. Fowler and Z. Chen, *Nat. Energy*, 2018, **3**, 279–289.
9 Z. Yang, J. Zhang, M. C. Kintner-Meyer, X. Lu, D. Choi, J. P. Lemmon and J. Liu, *Chem. Rev.*, 2011, **111**, 3577–3613.
10 P. De Luna, C. Hahn, D. Higgins, S. A. Jaffer, T. F. Jaramillo and E. H. Sargent, *Science*, 2019, **364**, 6438.
11 Y. Yang, *Nanoscale*, 2020, **12**, 3560–3573.
12 H. Zhong, C. Shi, J. Li, R. Yu, Q. Yu, H. Liu, Y. Yao, J. Wu, L. Zhou and L. Mai, *Chem. Commun.*, 2020, **56**, 4488–4491.
13 X. Z. Liu, T. Tang, W. J. Jiang, Q. H. Zhang, L. Gu and J. S. Hu, *Chem. Commun.*, 2020, **56**, 5374–5377.
14 H. Zhang, B. Zhang, Y. Yang, D. Ye, R. Chen, Q. Liao and X. Zhu, *Chem. Commun.*, 2021, **57**, 1258–1261.
15 J. Chang, G. Wang and Y. Yang, *Small Sci.*, 2021, **1**, 2100044.
16 M. Cui, X. Bai, J. Zhu, C. Han, Y. Huang, L. Kang, C. Zhi and H. Li, *Energy Storage Mater.*, 2021, **36**, 427–434.
17 K. Liang, L. Li and Y. Yang, *ACS Energy Lett.*, 2017, **2**, 373–390.
18 C. Li, M. Iqbal, J. Lin, X. Luo, B. Jiang, V. Malgras, K. C. Wu, J. Kim and Y. Yamauchi, *Acc. Chem. Res.*, 2018, **51**, 1764–1773.
19 H. Tian, Z. Li, G. Feng, Z. Yang, D. Fox, M. Wang, H. Zhou, L. Zhai, A. Kushima, Y. Du, Z. Feng, X. Shan and Y. Yang, *Nat. Commun.*, 2021, **12**, 237.
20 H. Tian, G. Feng, Q. Wang, Z. Li, W. Zhang, M. Lucero, Z. Feng, Z. L. Wang, Y. Zhang, C. Zhen, M. Gu, X. Shan and Y. Yang, *Nat. Commun.*, 2022, **13**, 7922.
21 J. Fu, Z. P. Cano, M. G. Park, A. Yu, M. Fowler and Z. Chen, *Adv. Mater.*, 2017, **29**, 1604685.
22 T. Zhou, N. Zhang, C. Wu and Y. Xie, *Energy Environ. Sci.*, 2020, **13**, 1132–1153.
23 J. Zheng, D. C. Bock, T. Tang, Q. Zhao, J. Yin, K. R. Tallman, G. Wheeler, X. Liu, Y. Deng, S. Jin, A. C. Marschilok, E. S. Takeuchi, K. J. Takeuchi and L. A. Archer, *Nat. Energy*, 2021, **6**, 398–408.
24 W. Sun, F. Wang, B. Zhang, M. Zhang, V. Küpers, X. Ji, C. Theile, P. Bieker, K. Xu, C. Wang and M. Winter, *Science*, 2021, **371**, 46–51.
25 H. Ge, X. Feng, D. Liu and Y. Zhang, *Nano Res. Energy*, 2023, **2**, e9120039.
26 Y. Tian, S. Chen, Y. He, Q. Chen, L. Zhang and J. Zhang, *Nano Res. Energy*, 2022, **1**, e9120025.
27 Y. Li, J. Fu, C. Zhong, T. Wu, Z. Chen, W. Hu, K. Amine and J. Lu, *Adv. Energy Mater.*, 2019, **9**, 1802605.
28 J. Fu, R. Liang, G. Liu, A. Yu, Z. Bai, L. Yang and Z. Chen, *Adv. Mater.*, 2019, **31**, e1805230.
29 F. Cheng and J. Chen, *Chem. Soc. Rev.*, 2012, **41**, 2172–2192.
30 T. P. Dirkse and N. A. Hampson, *Electrochim. Acta*, 1972, **17**, 383–386.
31 R. J. Gilliama, J. W. Graydon, D. W. Kirk and S. J. Thorpe, *Int. J. Hydrogen Energy*, 2007, **32**, 359–364.
32 Y. Li and H. Dai, *Chem. Soc. Rev.*, 2014, **43**, 5257–5275.
33 S. Liu, W. Han, B. Cui, X. Liu, F. Zhao, J. Stuart and S. Licht, *J. Power Sources*, 2017, **342**, 435–441.
34 M. Li, B. Liu, X. Fan, X. Liu, J. Liu, J. Ding, X. Han, Y. Deng, W. Hu and C. Zhong, *ACS Appl. Mater. Interfaces*, 2019, **11**, 28909–28917.
35 J. Park, M. Park, G. Nam, J. S. Lee and J. Cho, *Adv. Mater.*, 2015, **27**, 1396–1401.
36 C. Lin, S. S. Shinde, X. Li, D. H. Kim, N. Li, Y. Sun, X. Song, H. Zhang, C. H. Lee, S. U. Lee and J. H. Lee, *ChemSusChem*, 2018, **11**, 3215–3224.
37 M. T. Tsehaye, F. Alloin, C. Iojoiu, R. A. Tufa, D. Aili, P. Fischer and S. Velizarov, *J. Power Sources*, 2020, **475**, 228689.
38 Z. Li, W. Niu, Z. Yang, N. Zaman, W. Samarakoon, M. Wang, A. Kara, M. Lucero, M. V. Vyas, H. Cao, H. Zhou, G. E. Sterbinsky, Z. Feng, Y. Du and Y. Yang, *Energy Environ. Sci.*, 2020, **13**, 884–895.
39 Z. Li, Q. Wang, X. Bai, M. Wang, Z. Yang, Y. Du, G. E. Sterbinsky, D. Wu, Z. Yang, H. Tian, F. Pan, M. Gu, Y. Liu, Z. Feng and Y. Yang, *Energy Environ. Sci.*, 2021, **14**, 5035–5043.
40 J. Chang, G. Wang, X. Chang, Z. Yang, H. Wang, B. Li, W. Zhang, L. Kovarik, Y. Du, N. Orlovskaya, B. Xu, G. Wang and Y. Yang, *Nat. Commun.*, 2023, **14**, 1346.
41 J. Chang, G. Wang, M. Wang, Q. Wang, B. Li, H. Zhou, Y. Zhu, W. Zhang, M. Omer, N. Orlovskaya, Q. Ma, M. Gu, Z. Feng, G. Wang and Y. Yang, *Nat. Energy*, 2021, **6**, 1144–1153.
42 J. Chang, G. Wang, C. Li, Y. He, Y. Zhu, W. Zhang, M. Sajid, A. Kara, M. Gu and Y. Yang, *Joule*, 2023, **7**, 587–602.
43 G. Wang, J. Chang, S. Koul, A. Kushima and Y. Yang, *J. Am. Chem. Soc.*, 2021, **143**, 11595–11601.
44 J. Chang, T.-J. Ko, M. Je, H.-S. Chung, S. S. Han, M. S. Shawkat, M. Wang, S. J. Park, S. M. Yu, T.-S. Bae, M.-W. Moon, K. H. Oh, H. Choi, Y. Yang and Y. Jung, *ACS Energy Lett.*, 2021, **6**, 3481–3487.
45 J. Chang, L. Feng, K. Jiang, H. Xue, W.-B. Cai, C. Liu and W. Xing, *J. Mater. Chem. A*, 2016, **4**, 18607–18613.
46 J. Chang, S. Li, L. Feng, X. Qin and G. Shao, *J. Power Sources*, 2014, **266**, 481–487.
47 C. X. Zhao, J. N. Liu, J. Wang, D. Ren, J. Yu, X. Chen, B. Q. Li and Q. Zhang, *Adv. Mater.*, 2021, **33**, 2008606.
48 H. F. Wang, C. Tang, B. Wang, B. Q. Li and Q. Zhang, *Adv. Mater.*, 2017, **29**, 1702327.
49 X. F. Lu, Y. Chen, S. Wang, S. Gao and X. W. D. Lou, *Adv. Mater.*, 2019, **31**, 1902339.
50 X. Han, X. Ling, Y. Wang, T. Ma, C. Zhong, W. Hu and Y. Deng, *Angew. Chem., Int. Ed.*, 2019, **58**, 5359–5364.
51 F. Pan, Z. Li, Z. Yang, Q. Ma, M. Wang, H. Wang, M. Olszta, G. Wang, Z. Feng, Y. Du and Y. Yang, *Adv. Energy Mater.*, 2021, **11**, 2002204.
52 A. Krezel and W. Maret, *Arch. Biochem. Biophys.*, 2016, **611**, 3–19.
53 M. Bockelmann, U. Kunz and T. Turek, *Electrochem. Commun.*, 2016, **69**, 24–27.
54 W. Zhang, J. Chang, G. Wang, Z. Li, M. Wang, Y. Zhu, B. Li, H. Zhou, G. Wang, M. Gu, Z. Feng and Y. Yang, *Energy Environ. Sci.*, 2022, **15**, 1573–1584.
55 L. An, Z. Zhang, J. Feng, F. Lv, Y. Li, R. Wang, M. Lu, R. B. Gupta, P. Xi and S. Zhang, *J. Am. Chem. Soc.*, 2018, **140**, 17624–17631.
56 A. A. Mohamad, *J. Power Sources*, 2006, **159**, 752–757.
57 T. T. Gebremariam, F. Chen, Q. Wang, J. Wang, Y. Liu, X. Wang and A. Qaseem, *ACS Appl. Energy Mater.*, 2018, **1**, 1612–1625.
58 Y. Li, M. Gong, Y. Liang, J. Feng, J. E. Kim, H. Wang, G. Hong, B. Zhang and H. Dai, *Nat. Commun.*, 2013, **4**, 1805.
59 S. Li, J. Shang, M. Li, M. Xu, F. Zeng, H. Yin, Y. Tang, C. Han and H. M. Cheng, *Adv. Mater.*, 2022, e2207115.
60 Y. Li and J. Lu, *ACS Energy Lett.*, 2017, **2**, 1370–1377.
61 Y. Bu, O. Gwon, G. Nam, H. Jang, S. Kim, Q. Zhong, J. Cho and G. Kim, *ACS Nano*, 2017, **11**, 11594–11601.
62 R. Cao, J.-S. Lee, M. Liu and J. Cho, *Adv. Energy. Mater.*, 2012, **2**, 816–829.
63 Z. Cui, G. Fu, Y. Li and J. B. Goodenough, *Angew. Chem., Int. Ed.*, 2017, **56**, 9901–9905.
64 X. Liu, M. Park, M. G. Kim, S. Gupta, G. Wu and J. Cho, *Angew. Chem., Int. Ed.*, 2015, **54**, 9654–9658.
65 Z. Pei, Z. Yuan, C. Wang, S. Zhao, J. Fei, L. Wei, J. Chen, C. Wang, R. Qi, Z. Liu and Y. Chen, *Angew. Chem., Int. Ed.*, 2020, **59**, 4793–4799.
66 K. W. Leong, Y. Wang, M. Ni, W. Pan, S. Luo and D. Y. C. Leung, *Renewable Sustainable Energy Rev.*, 2022, **154**, 111771.
67 M. Xiao, Z. Xing, Z. Jin, C. Liu, J. Ge, J. Zhu, Y. Wang, X. Zhao and Z. Chen, *Adv. Mater.*, 2020, **32**, 2004900.
68 J. Chang, G. Wang, Z. Yang, B. Li, Q. Wang, R. Kuliiev, N. Orlovskaya, M. Gu, Y. Du, G. Wang and Y. Yang, *Adv. Mater.*, 2021, **33**, 2101425.
69 F. Meng, H. Zhong, D. Bao, J. Yan and X. Zhang, *J. Am. Chem. Soc.*, 2016, **138**, 10226–10231.
70 R. Gao, J. Wang, Z.-F. Huang, R. Zhang, W. Wang, L. Pan, J. Zhang, W. Zhu, X. Zhang, C. Shi, J. Lim and J.-J. Zou, *Nat. Energy*, 2021, **6**, 614–623.
71 J. Zhang, Z. Zhao, Z. Xia and L. Dai, *Nat. Nanotechnol.*, 2015, **10**, 444–452.
72 Y. Yuan, J. Wang, S. Adimi, H. Shen, T. Thomas, R. Ma, J. P. Attfield and M. Yang, *Nat. Mater.*, 2020, **19**, 282–286.
73 G. W. Sievers, A. W. Jensen, J. Quinson, A. Zana, F. Bizzotto, M. Oezaslan, A. Dworzak, J. J. K. Kirkensgaard, T. E. L. Smitshuysen, S. Kadkhodazadeh, M. Juelsholt, K. M. O. Jensen, K. Anklam, H. Wan,

J. Schafer, K. Cepe, M. Escudero-Escribano, J. Rossmeisl, A. Quade, V. Bruser and M. Arenz, *Nat. Mater.*, 2021, **20**, 208–213.
74 Y. Yang, S. P. Albu, D. Kim and P. Schmuki, *Angew. Chem., Int. Ed.*, 2011, **50**, 9071–9075.
75 Y. Yang, K. Lee, M. Zobel, M. Mackovic, T. Unruh, E. Spiecker and P. Schmuki, *Adv. Mater.*, 2012, **24**, 1571–1575.
76 Y. Yang, D. Kim and P. Schmuki, *Electrochem. Commun.*, 2011, **13**, 1021–1025.
77 Y. Yang, H. Fei, G. Ruan, L. Li, G. Wang, N. D. Kim and J. M. Tour, *ACS Appl. Mater. Interfaces*, 2015, **7**, 20607–20611.
78 K. Liang, L. Guo, K. Marcus, S. Zhang, Z. Yang, D. E. Perea, L. Zhou, Y. Du and Y. Yang, *ACS Catal.*, 2017, **7**, 8406–8412.
79 K. Liang, S. Pakhira, Z. Yang, A. Nijamudheen, L. Ju, M. Wang, C. I. Aguirre-Velez, G. E. Sterbinsky, Y. Du, Z. Feng, J. L. Mendoza-Cortes and Y. Yang, *ACS Catal.*, 2018, **9**, 651–659.
80 J. Chang, G. Wang, A. Belharsa, J. Ge, W. Xing and Y. Yang, *Small Methods*, 2020, **4**, 1900632.
81 Z. Li, W. Niu, L. Zhou and Y. Yang, *ACS Energy Lett.*, 2018, **3**, 892–898.
82 K. Liang, Y. Yan, L. Guo, K. Marcus, Z. Li, L. Zhou, Y. Li, R. Ye, N. Orlovskaya, Y.-H. Sohn and Y. Yang, *ACS Energy Lett.*, 2017, **2**, 1315–1320.
83 L. Shi, W. Zhou, Z. Li, S. Koul, A. Kushima and Y. Yang, *ACS Nano*, 2018, **12**, 6335–6342.
84 Y. Yang, H. Fei, G. Ruan, Y. Li and J. M. Tour, *Adv. Funct. Mater.*, 2015, **25**, 6199–6204.
85 Y. Yang, H. Fei, G. Ruan and J. M. Tour, *Adv. Mater.*, 2015, **27**, 3175–3180.
86 Z. Li, W. Niu, Z. Yang, A. Kara, Q. Wang, M. Wang, M. Gu, Z. Feng, Y. Du and Y. Yang, *Energy Environ. Sci.*, 2020, **13**, 3110–3118.
87 Y. Yang, D. Kim, M. Yang and P. Schmuki, *Chem. Commun.*, 2011, **47**, 7746–7748.
88 Y. Yang, H. Fei, G. Ruan, C. Xiang and J. M. Tour, *Adv. Mater.*, 2014, **26**, 8163–8168.
89 Y. Yang, D. Kim and P. Schmuki, *Chem. – Asian J.*, 2011, **6**, 2916–2919.
90 K. Liang, K. Marcus, Z. Yang, L. Zhou, H. Pan, Y. Bai, Y. Du, M. H. Engelhard and Y. Yang, *Small*, 2018, **14**, 1702295.
91 Y. Yang, D. Kim and P. Schmuki, *Electrochem. Commun.*, 2011, **13**, 1198–1201.
92 K. Liang, L. Ju, S. Koul, A. Kushima and Y. Yang, *Adv. Energy. Mater.*, 2019, **9**, 1802543.
93 J. Chang, G. Wang, W. Zhang and Y. Yang, *J. Energy Chem.*, 2022, **68**, 439–453.
94 L. Guo, J. Deng, G. Wang, Y. Hao, K. Bi, X. Wang and Y. Yang, *Adv. Funct. Mater.*, 2018, **28**, 1804540.
95 K. Marcus, K. Liang, W. Niu and Y. Yang, *J. Phys. Chem. Lett.*, 2018, **9**, 2746–2750.
96 W. Niu, Z. Li, K. Marcus, L. Zhou, Y. Li, R. Ye, K. Liang and Y. Yang, *Adv. Energy. Mater.*, 2018, **8**, 1701642.
97 W. Niu, S. Pakhira, K. Marcus, Z. Li, J. L. Mendoza-Cortes and Y. Yang, *Adv. Energy. Mater.*, 2018, **8**, 1800480.
98 W. Niu and Y. Yang, *ACS Appl. Energy Mater.*, 2018, **1**, 2440–2445.
99 G. Wang, Z. Yang, Y. Du and Y. Yang, *Angew. Chem., Int. Ed.*, 2019, **58**, 15848–15854.
100 N. M. Markovic and H. A. Gasteiger, *J. Phys. Chem.*, 1996, **100**, 6715–6721.
101 H. C. Shin, J. Dong and M. Liu, *Adv. Mater.*, 2003, **15**, 1610–1614.
102 M. J. Byungkwon Lim, Pedro H. C. Camargo, Eun Chul Cho, Jing Tao, Xianmao Lu, Yimei Zhu and Younan Xia, *Science*, 2009, **324**, 1302–1305.
103 N. Z. Lingzheng Bu, Shaojun Guo, Xu Zhang, Jing Li, Jianlin Yao, Tao Wu, Gang Lu, Jing-Yuan Ma, Dong Su and Xiaoqing Huang, *Science*, 2016, **354**, 1410–1414.
104 X. Tian, X. Zhao, Y.-Q. Su, L. Wang, H. Wang, D. Dang, B. Chi, H. Liu, E. J. M. Hensen, X. W. D. Lou and B. Y. Xia, *Science*, 2019, **366**, 850–856.
105 M. Li, Z. Zhao, T. Cheng, A. Fortunelli, C.-Y. Chen, R. Yu, Q. Zhang, L. Gu, B. V. Merinov, Z. Lin, E. Zhu, T. Yu, Q. Jia, J. Guo, L. Zhang, W. A. Goddard, I. I. I. Yu Huang and X. Duan, *Science*, 2016, **354**, 1414–1419.
106 M. Luo, Z. Zhao, Y. Zhang, Y. Sun, Y. Xing, F. Lv, Y. Yang, X. Zhang, S. Hwang, Y. Qin, J. Y. Ma, F. Lin, D. Su, G. Lu and S. Guo, *Nature*, 2019, **574**, 81–85.
107 M. K. Debe, *Nature*, 2012, **486**, 43–51.
108 G. Li, L. Feng, J. Chang, B. Wickman, H. Gronbeck, C. Liu and W. Xing, *ChemSusChem*, 2014, **7**, 3374–3381.
109 Q. Lv, J. Chang, W. Xing and C. Liu, *RSC Adv.*, 2014, **4**, 32997–33000.
110 J. Chang, L. Feng, C. Liu and W. Xing, *ChemSusChem*, 2015, **8**, 3340–3347.
111 L. Feng, K. Li, J. Chang, C. Liu and W. Xing, *Nano Energy*, 2015, **15**, 462–469.
112 L. Yang, G. Li, R. Ma, S. Hou, J. Chang, M. Ruan, W. Cai, Z. Jin, W. Xu, G. Wang, J. Ge, C. Liu and W. Xing, *Nano Res.*, 2021, **14**, 2853–2860.
113 Y. Zhou, Q. Wang, X. Tian, J. Chang and L. Feng, *J. Energy Chem.*, 2022, **75**, 46–54.
114 Y. Zhou, L. Yu, J. Chang, L. Feng and J. Zhang, *Green Energy Environ.*, 2022, DOI: 10.1016/j.gee.2022.08.007.
115 W. Xu, j Chang, Y. Cheng, H. Liu, J. Li, Y. Ai, Z. Hu, X. Zhang, Y. Wang, Q. Wang, Y. Yang and H. Sun, *Nano Res.*, 2021, **15**, 965–971.
116 W. Zhang, J. Chang and Y. Yang, *SusMat*, 2023, **3**, 2–20.
117 J. Chang, X. Sun, L. Feng, W. Xing, X. Qin and G. Shao, *J. Power Sources*, 2013, **239**, 94–102.
118 K. Wang, B. Wang, J. Chang, L. Feng and W. Xing, *Electrochim. Acta*, 2014, **150**, 329–336.
119 L. Yan, S. Yao, J. Chang, C. Liu and W. Xing, *J. Power Sources*, 2014, **250**, 128–133.
120 L. Feng, J. Chang, K. Jiang, H. Xue, C. Liu, W.-B. Cai, W. Xing and J. Zhang, *Nano Energy*, 2016, **30**, 355–361.
121 K. Jiang, J. Chang, H. Wang, S. Brimaud, W. Xing, R. J. Behm and W. B. Cai, *ACS Appl. Mater. Interfaces*, 2016, **8**, 7133–7138.
122 S. Wang, J. Chang, H. Xue, W. Xing and L. Feng, *ChemElectroChem*, 2017, **4**, 1243–1249.
123 L. Yang, G. Li, J. Chang, J. Ge, C. Liu, F. Vladimir, G. Wang, Z. Jin and W. Xing, *Appl. Catal., B*, 2020, **260**, 118200.
124 T. W. van Deelen, C. Hernández Mejía and K. P. de Jong, *Nat. Catal.*, 2019, **2**, 955–970.
125 M. Jiao, Q. Zhang, C. Ye, Z. Liu, X. Zhong, J. Wang, C. Li, L. Dai, G. Zhou and H. M. Cheng, *Proc. Natl. Acad. Sci. U. S. A.*, 2022, **119**, e2202202119.
126 X. Qin, Z. Wang, J. Han, Y. Luo, F. Xie, G. Cui, X. Guo and X. Sun, *Chem. Commun.*, 2018, **54**, 7693–7696.
127 J. Gao, J. Wang, L. Zhou, X. Cai, D. Zhan, M. Hou and L. Lai, *ACS Appl. Mater. Interfaces*, 2019, **11**, 10364–10372.
128 C. Xia, L. Huang, D. Yan, A. I. Douka, W. Guo, K. Qi and B. Y. Xia, *Adv. Funct. Mater.*, 2021, **31**, 2105021.
129 D. Ji, L. Fan, L. Li, S. Peng, D. Yu, J. Song, S. Ramakrishna and S. Guo, *Adv. Mater.*, 2019, **31**, 1808267.
130 Q. Jin, B. Ren, J. Chen, H. Cui and C. Wang, *Appl. Catal., B*, 2019, **256**, 117887.
131 Q. Lu, X. Zou, K. Liao, R. Ran, W. Zhou, M. Ni and Z. Shao, *Carbon Energy*, 2020, **2**, 461–471.
132 A. Baby, D. Singh, C. Murugesan and P. Barpanda, *Chem. Commun.*, 2020, **56**, 8400–8403.
133 Y. Chen, W. Zhang, Z. Zhu, L. Zhang, J. Yang, H. Chen, B. Zheng, S. Li, W. Zhang, J. Wu and F. Huo, *J. Mater. Chem. A*, 2020, **8**, 7184–7191.
134 Y. Cheng, F. Liao, W. Shen, L. Liu, B. Jiang, Y. Li and M. Shao, *Nanoscale*, 2017, **9**, 18977–18982.
135 X. Yan, Y. Ha and R. Wu, *Small Methods*, 2021, **5**, 2000827.
136 Z. Guan, X. Zhang, W. Chen, J. Pei, D. Liu, Y. Xue, W. Zhu and Z. Zhuang, *Chem. Commun.*, 2018, **54**, 12073–12076.
137 H. Li, L. Ma, C. Han, Z. Wang, Z. Liu, Z. Tang and C. Zhi, *Nano Energy*, 2019, **62**, 550–587.

